Spring 2022

Quantifying the Controls of Shear-Coupled P-Waves

Jackson Saftner

Quantifying the Controls of Shear-Coupled P-waves

By

Jackson Saftner

Bachelor of Science
University of South Carolina, 2021

Submitted in Partial Fulfillment of the Requirements

For the Degree of Master of Science in

Geological Sciences

College of Arts and Sciences

University of South Carolina

2022

Accepted by:

Thomas J. Owens, Director of Thesis

Scott White, Reader

Philip Crotwell, Reader

George Randall, Reader

Tracey L. Weldon, Vice Provost and Dean of the Graduate School

Acknowledgments

I would like to thank Dr. Thomas Owens for serving as my advisor and providing guidance throughout this project. I would also like to thank my other committee members, Dr. Scott White, Dr. Philip Crotwell, and Dr. George Randall, for serving as advisors and contributing to my education in geophysics. Finally, a note of gratitude for my family and friends, who have supported me throughout the course of this project.

Abstract

Shear-coupled P-waves have been shown to possess great utility in resolving crustal and upper mantle models, however these phases remain largely untapped due to their ephemeral nature. Shear-coupled P-waves are a type of seismic phase that undergo S-to-P conversion either at the free-surface or at the base of the crust. Under the proper conditions, it is possible for the converted crustal P phases to achieve total internal reflection, allowing these phases to remain large in amplitude and sample long segments of the crust. In this study, we use a combination of real-world observations collected from literature, and synthetic seismograms, to constrain the parameters that allow for observable shear-coupled P-waves to be generated.

The primary controls we investigate are source distance, source depth, and teleseismic S-wave polarization. By examining observations within real data and generating synthetic seismograms, we find that for epicentral distances between 32 and 55 degrees, the incoming S-wave has an angle of incidence that allows for converted phases to achieve total internal reflection; source depths greater than 100km produce depth phases that do not interfere with the S-coda; and incoming S-waves that are more vertically polarized convert more energy into crustal P-waves. After determining the range of parameters that reliably produce observable shear-coupled P-waves, we then develop an atlas of locations where shear-coupled P-waves are most likely to be observed.

Finally, we use our atlas of shear-coupled P-wave observability, informed by our newly constrained controls, to search preexisting data for new observations of shear-coupled P-waves.

Table of Contents

List of Figures

List of Tables

Chapter 1: Introduction

Shear-coupled P-waves are ephemeral teleseismic phases that can grow to large amplitudes under conditions that allow for P-waves to be totally internally reflected within the crust. Shear-coupled P-waves describe several phases in the S coda, all of which travel through the mantle as S-waves and undergo S-to-P conversion, either at the free surface or at the Moho (Figure 1.1). These phases have been shown to possess great potential in probing the crust and upper mantle.

Sp, the seismic phase that travels through the mantle as an S-wave and is converted into an upgoing P-wave at the at the Moho, arrives before the direct S-wave (Figure 1.1). This phase has been studied and utilized for decades. In places like Eastern Canada (Jordan & Frazer, 1975), as well as in the Tibetan Plateau (Owens & Zandt, 1997), *Sp* has been used to calculate crustal thicknesses. Additionally, under the right conditions, similar phases can be created at upper mantle discontinuities, allowing us to further resolve our models of the upper mantle beneath the Eastern US (Zandt & Randall, 1985).

SsPmp travels to the free surface as an S-wave, where it is then converted to a downgoing P-wave, and finally reflected off the Moho to the receiver (Figure 1.1). If the angle of incidence (defined from the vertical (Figure 1.1)) of the incoming S-wave is high enough, the P-wave generated by conversion at the free surface can become trapped within the crust through total internal reflection.

Total internal reflection results in high amplitude P arrivals that follow the main S arrival because the downgoing energy is entirely trapped within the crust, except for energy lost as S-waves transmitted into the mantle. In addition to total internal reflection, *SsPmp* also undergoes constructive interference with *SpSmp* (Figure 1.1). Another consequence of total internal reflection is that multiply reflected crustal P-waves arrive with large amplitudes, and those phases can sample hundreds of kilometers of crust. Using this property of total internal reflection, studies like Owens & Zandt (1997) and Thompson et al. (2019) phases like *SsPmp* and *SsPmpPmp* were utilized to calculate bulk crustal properties across large segments of crust.

In this project we narrow the controls on shear-coupled P-wave observability through comparison of previously recorded shear-coupled P-waves in the literature with synthetic seismograms produced using code developed by Randall (1994), which is based on Kennett's (1983) reflection matrix approach. Using verified recordings from literature as a control, we calculate synthetics to investigate the source parameters and station distances that allow for the observation of uncomplicated shear-coupled P-waves. Additionally, using our newly constrained controls, we develop an atlas of locations where shear-coupled P-waves are likely to be recorded. Finally, we use our controls and our map to search for shear-coupled P-waves within data recorded by the seismic station WRAB in Australia.

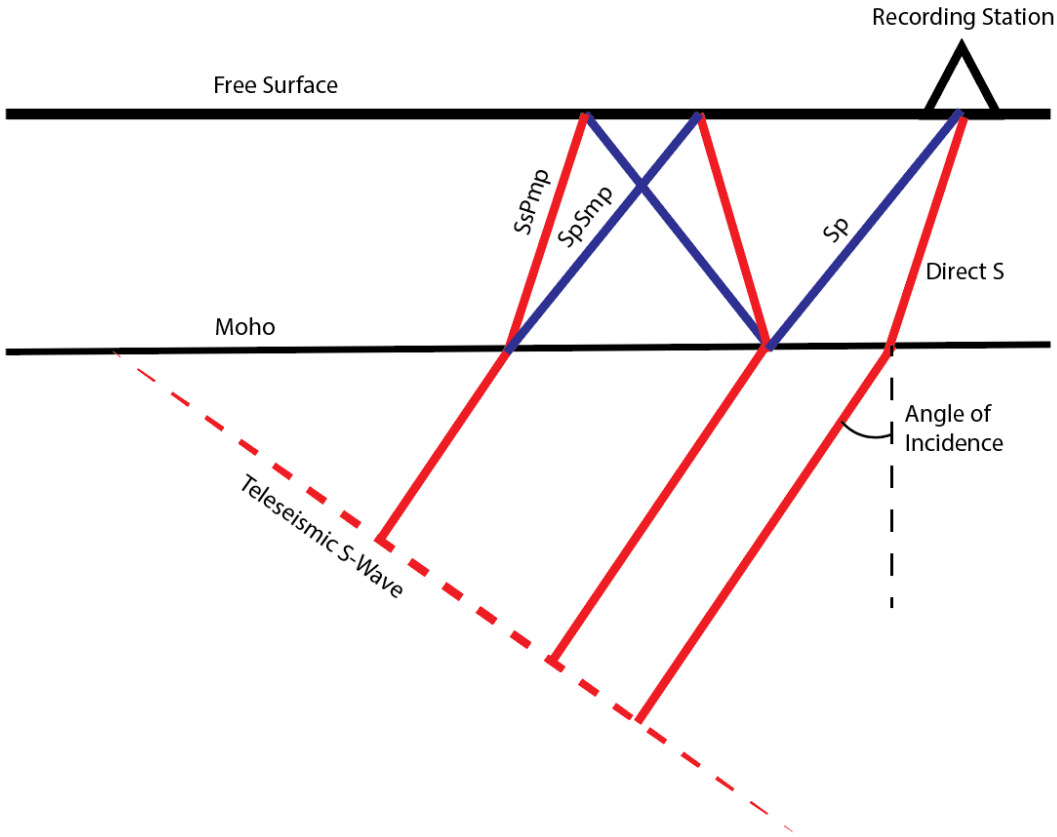

Figure 1.1. A schematic diagram of shear-coupled P-waves. All phases originate from the same planewave. Red lines show S-wave portions of a raypath, while blue lines denote P-wave portions of a raypath. We also include the angle of incidence of the teleseismic S-wave, showing that it is measured as the angle from the vertical. Note that we assume a flat earth in this example.

Chapter 2: Controls on Shear-coupled P-Waves

1.1 Source Distance

The path that a seismic ray will take through the earth is determined by its ray parameter as well as the properties of the medium through which it travels. Oftentimes referred to as "horizontal slowness", the ray parameter "p" for a particular ray must remain constant along its path to obey Snell's law:

$$\frac{Sin(i_1)}{V_1} = \frac{Sin(i_2)}{V_2} = p$$

where "i" represents the angle of incidence, measured from vertical (Figure 1.1), and "V" represents the seismic velocity of a layer. Note that this representation of Snell's law assumes a flat earth for demonstration purposes.

At any seismic interface, the energy of an incoming ray can be transmitted or reflected as either a P-wave or an S-wave. Using the Moho as an example:

$$\frac{Sin(i_{s-mantle})}{V_{s-mantle}} = \frac{Sin(i_{p-mantle})}{V_{p-mantle}} = \frac{Sin(i_{s-crust})}{V_{s-crust}} = \frac{Sin(i_{p-crust})}{V_{p-crust}} = p$$

where the subscripts of "i" and "V" denote the layer that the wave is traveling through as well as its phase type. For the purposes of our study there are two important ray parameters to consider:

$$p_1 = \frac{1}{V_{p-mantle}} \qquad \& \qquad p_2 = \frac{1}{V_{p-crust}}$$

which describe the rays that will produce critically refracted waves that propagate along the base of the Moho (p_1) and the top of the Moho (p_2) as p-waves. The ray parameters valued between p_1 and p_2 achieve total internal reflection.

The ray path of p_1 is shown in Figure 2.1 (middle), where an incoming S-wave, with an angle of incidence "i_{cd}", produces crustal phases that are then critically refracted at the Moho. The distance at which this ray is recorded is called the critical distance. Rays with S-waves emerging from the mantle at angles of incidence smaller than i_{cd} (Figure 2.1, bottom) appear beyond the critical distance, and allow energy to escape from the crust back into the mantle. This region, beyond p_1, is called the pre-critical regime. If the angle of incidence is greater than i_{cd}, the energy transmitted into the crust will achieve total internal reflection (Figure 2.1, top). The collection of ray parameters that achieve this total internal reflection fall into what is known as the post-critical regime.

p_2 is critically refracted as it converts from a mantle S-wave to a crustal P-wave. Rays that emerge at distances smaller than the distance at which p_2 emerges will be reflected off the bottom of the Moho and not enter the crust as P-waves.

In a later section, we calculate synthetic seismograms for a range of distances, using the ak135 velocity model (Kennett et al., 1995), and find that the critical distance (for p_1) falls around 55 degrees. Additionally, converted P-waves were recorded in our synthetics at distances as close as 20 degrees, meaning that p_2 emerges at some distance less than 20 degrees. At around 32 degrees, it is possible for surface waves and crustal multiples to begin complicating the S-coda, so we choose this distance as the

lower bound of distances. For the purposes of identifying regions where shear-coupled P-waves can be observed, we select 32 to 55 degrees as our distance window.

1.2 Source Depth

Another important consideration when searching for clear, uncomplicated, shear-coupled P-wave arrivals is the depth of the source. If the source is too shallow, source side reverberations, produced by upgoing energy being reflected back down into the earth, tend to follow too closely to the main S arrival, complicating the coda. If the depth of the event is greater than 100 km, the delay between the arrival of the main S-wave and the depth phases is long enough to allow for uncomplicated shear-coupled P-wave waveforms (Figure 2.2).

There are other seismic phases that have a high potential for interfering with the S coda, such as the global phases *PcS* and *ScP*. While sufficiently deep sources will delay depth phases at all distances, global phases cause interference at certain distances regardless of source depth. At shallow depths, *PcS* and *ScP* complicate shear-coupled P-wave arrivals at distances around 40 degrees. As depth increases, *ScP* begins to interfere at smaller distances and *PcS* begins to interfere at greater distances. The same is true of *PKiKP* and its depth phases, except instead of causing interference near 40 degrees, these phases cause interference near the pre-critical regime around 54 degrees. (Figure 2.2) Fortunately, these phases arrive with small amplitudes relative to the main S-wave (Yu et al., 2012).

Being unable to avoid the influence of these global phases, we simply note that there is the potential for interference. Our cutoff for depth is therefore defined by the

depth at which source reverberations are removed from the thirty seconds following the direct S arrival, around 100km.

1.3 Shear Wave Polarization

Another factor to consider when searching for large amplitude shear-coupled P-waves is that, for sufficient energy to be converted into crustal P-waves, the incoming mantle shear wave must have particle motion with some vertical component. At a seismic interface, a horizontally polarized shear wave will only generate a shear wave in the next layer, while a vertically polarized shear wave will transfer some component of its energy into the next layer as a P-wave.

Each seismic event has a unique radiation pattern that describes the direction and intensity of P and S-waves generated at the source (Figure 2.3). Radiation patterns can also describe the polarization of S-waves for each point on a focal sphere. Due to the unique distribution of P and S energy at each source, the observability of shear-coupled P-waves varies with distance from the source as well as azimuth.

For the purposes of this study, we use a value of 0.3 as our control. This value was selected by examining previously recorded observations and their Sv coefficients, which are discussed later. We note that any Sv coefficient greater than zero could convert a portion of its energy into crustal P-waves, but in practice, values below 0.3 produce phases that are easily lost in ambient noise.

1.4 Source Magnitude

Additionally, magnitude will have an impact on observability, but only in the sense that larger events generally produce larger phases. Any event could produce an observable shear-coupled P-wave provided the magnitude of that event is large enough to generate arrivals above the receiver station's ambient noise level. Once again, for the purposes of this study, we rely on previous observations to define our cutoff value for magnitude, which is 5.5.

1.5 Summary of Controls

In summation, the primary controls on shear-coupled P-wave observability are epicentral distance, depth, and S-wave polarization. Distances that fall within the post-critical regime, or closer than about 55 degrees. We also do not include distances less than 32 degrees in order to avoid interference from surface waves and crustal multiples. Sources at shallow depths will produce depth phases that arrive within 30 seconds of the direct S arrival, and for that reason, we do not expect clear shear-coupled P-wave observations from events with source depths less than 100km. Finally, in order for S-to-P conversion to occur at the base of the crust, the incoming S-wave must have a component of its energy vertically polarized. Observations pulled from the literature, suggest that rays with Sv coefficients less than 0.3 are unlikely to produce clear shear-coupled P-waves.

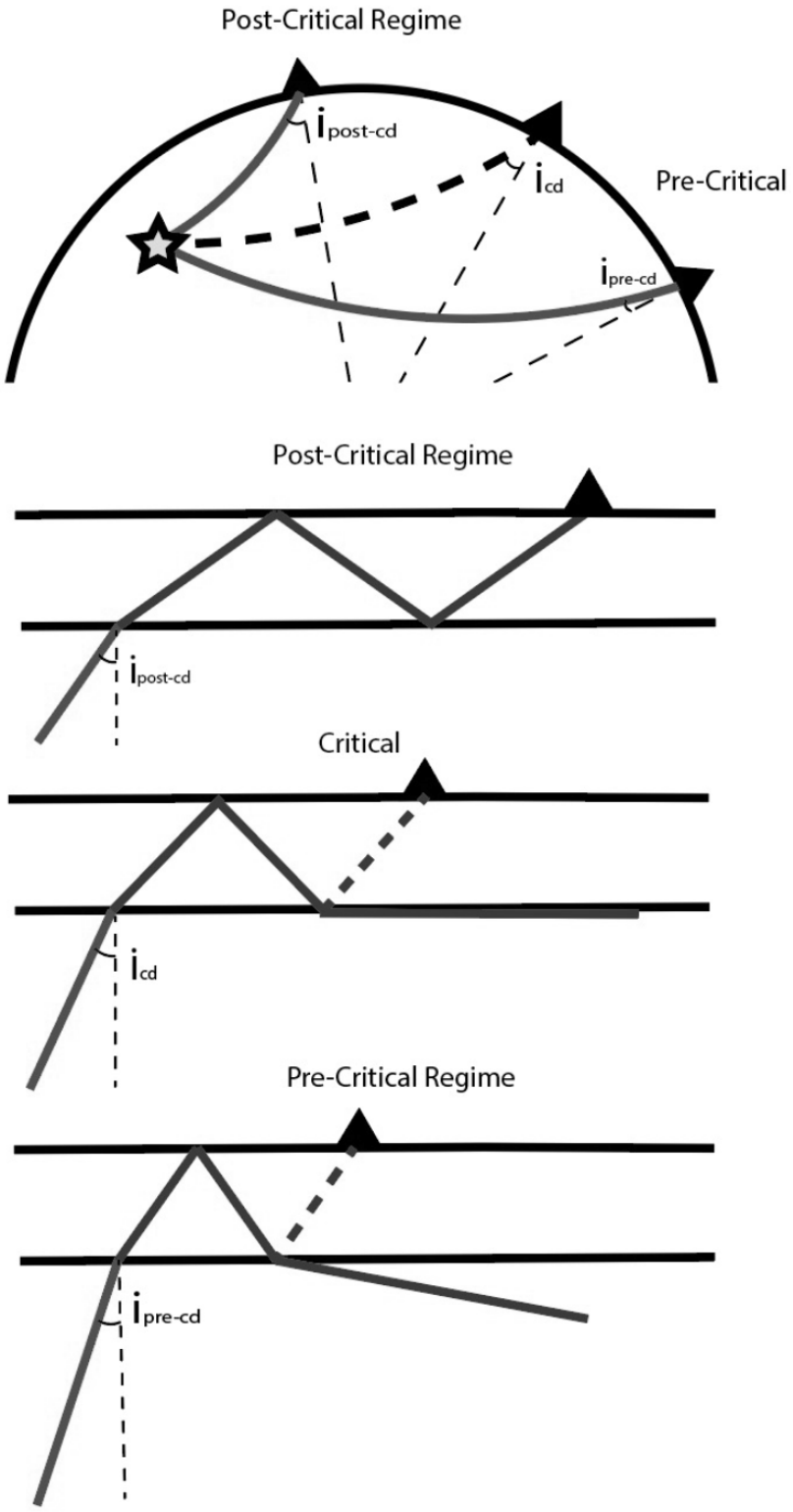

Figure 2.1. Schematic diagram of pre- and post-critical regimes on a curve earth (Top) and zoomed in sections within each regime (Bottom three). As distance from the source (star) increases, the angle "I" becomes smaller.

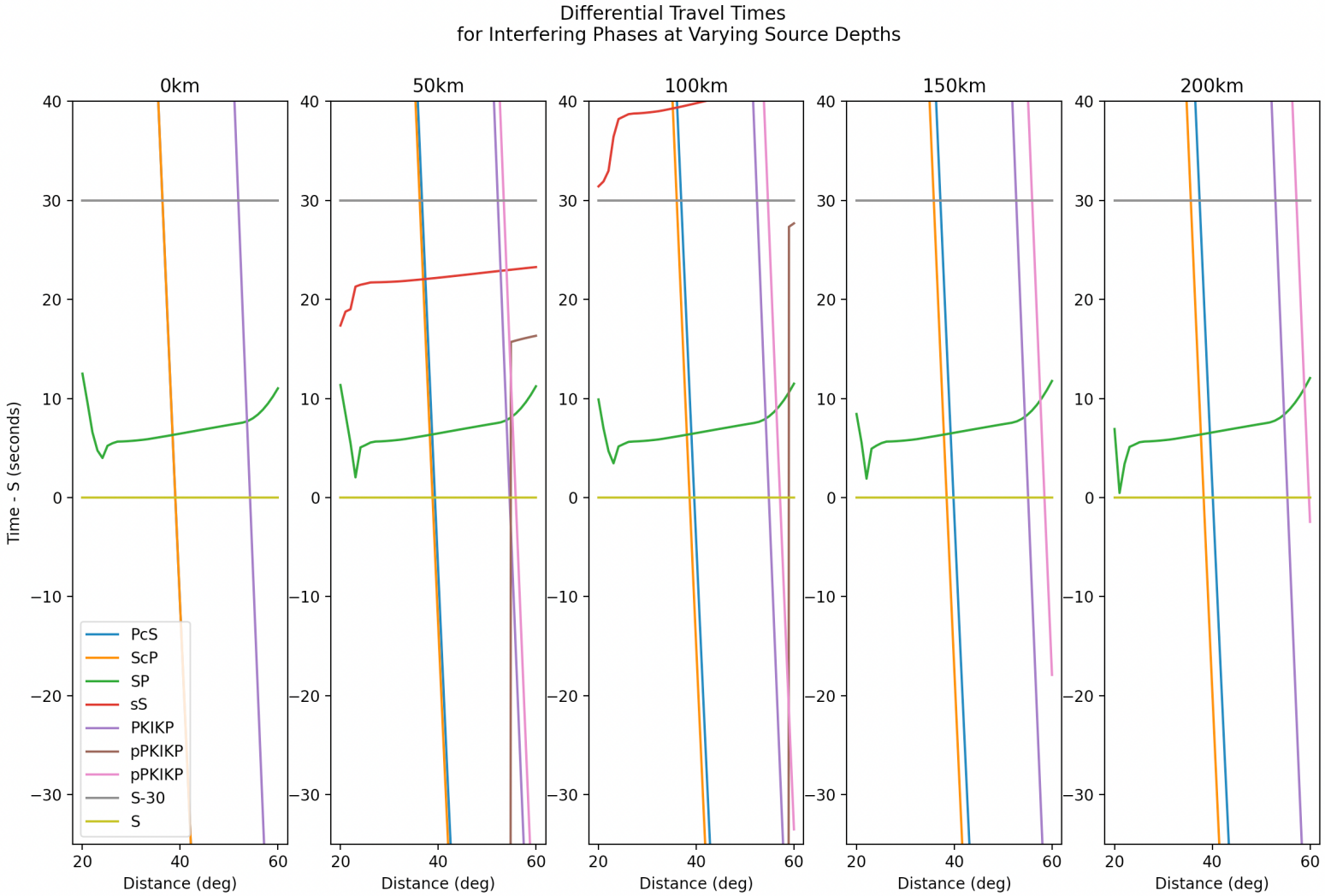

Figure 2.2. Differential travel time curves for interfering phases produced at various depths. All times are given relative to the direct S-wave. Those phases that fall between the curves for S and S-30 are likely to complicate the observation of shear-coupled P-waves.

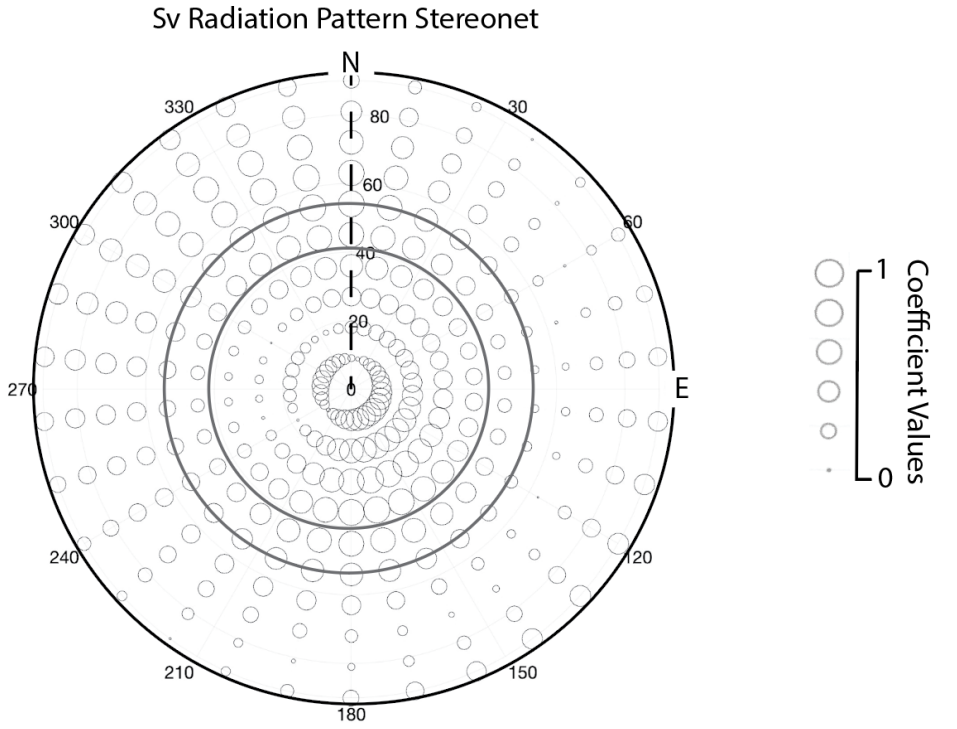

Figure 2.3) A stereonet showing the Sv coefficients for event 2013-10-01 (Table 1). The center of this plot represents the coefficients for a downward going ray, while the outer edge describes rays leaving the source horizontally. Two small circles bound the rays that satisfy our distance control. The inner most circle shows takeoff angles that land around 60 degrees from the source, while the larger circle shows takeoff angles that land near 30 degrees from the source. Larger points indicate directions where the generation of vertically polarized S-waves are produced with greater amplitudes. The smallest points show directions where S-waves are either not generated, or generated but polarized horizontally.

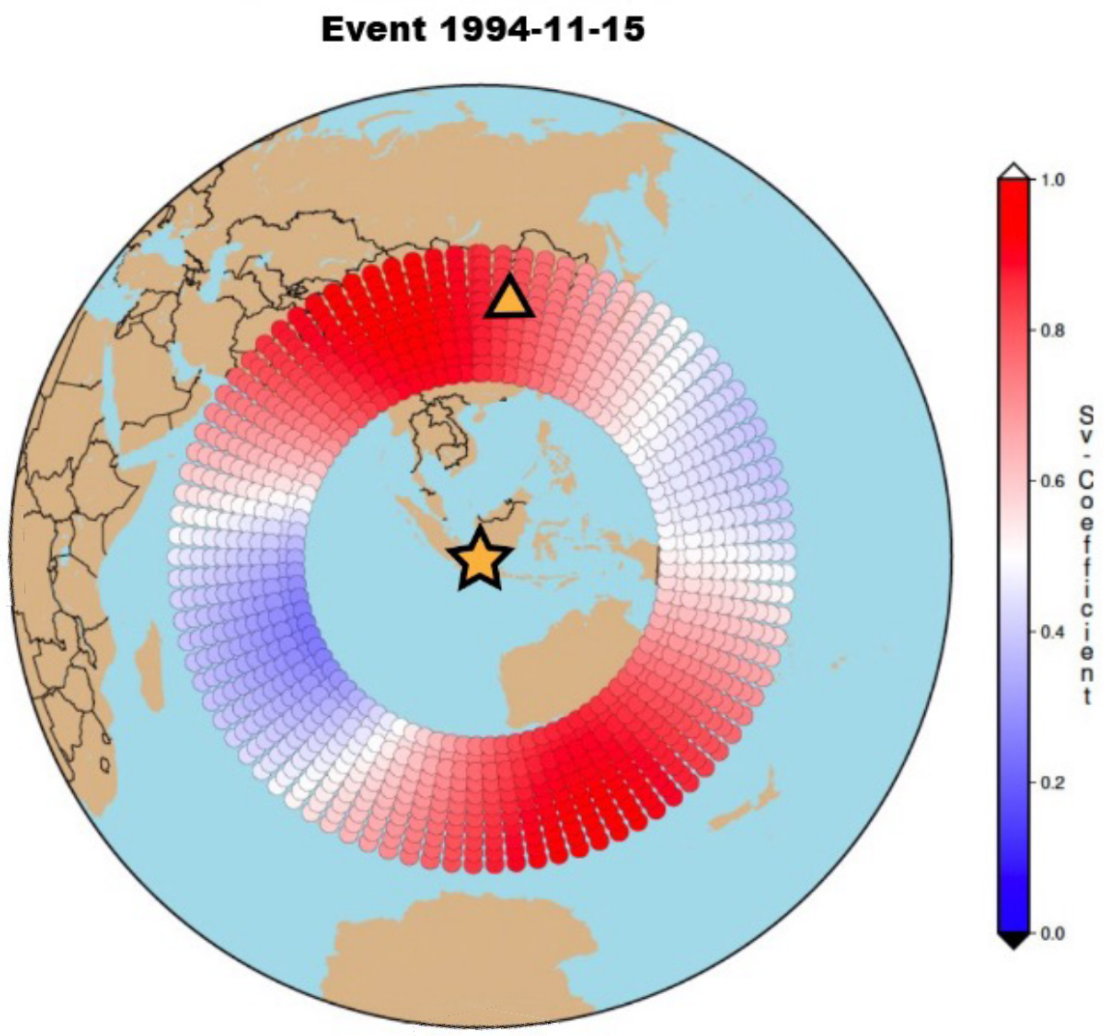

Figure 2.4 A single event sweet spot map. Values in red represent a high degree of vertical polarization and are likely to produce better shear-coupled P-waves. Each point shares a constant radius that was selected for stylist purposes. The source location (at a depth of 570.7km) is shown as a star and station BJT is represented by a triangle. (Station BJT is the location of a shear-coupled P-wave recording for this event) Each dot represents a value projected from a point on the radiation pattern's focal sphere to the base of the crust.

Chapter 3: Methods

2.1 Sweet Spot Maps

The first tools that we developed to constrain the controls on shear-coupled P-wave observation were sweet spot maps. These maps assist in visualizing the distribution of vertically polarized shear energy for a particular seismic source. Using code from Ou (2008), we can generate radiation patterns for any given seismic moment tensor, which give solutions for S and P coefficients at different azimuths and takeoff angles (Figure 2.3). These radiation patterns also include the vertical and horizontal components of the S coefficient, Sv and Sh. The values of these coefficients at each point on the focal sphere range from 0 to 1. This number, when scaled by the magnitude of an event, describes the amplitude of the phase generated at a particular azimuth and takeoff angle.

After modeling the source radiation pattern, the solutions that are assigned to the focal sphere are projected, according to ray theory, through the earth and up to the base of the crust. This projection is accomplished using Taup, a travel time and raypath calculator developed by Crotwell et al. (1999). Given the depth of an earthquake, as well as a takeoff angle, Taup can determine a raypath through an earth that is modeled by the ak135 velocity model (Kennett et al., 1995). The solution then provides the epicentral distance from the event to the receiver. The takeoff angle is relevant to the points on a small circle in the focal sphere solution of the radiation pattern (Figure 2.3). Taking all the solutions that share a takeoff angle and projecting them the relevant distance calculated

by Taup, according to the azimuth of the solution on the focal sphere, yields a collection of points that represent the focal sphere solutions mapped to their emergence sites at the base of the crust. Points beyond 55 degrees are removed from the solutions because those points would be in the pre-critical regime (Figure 2.4). Points closer than 32 degrees are also removed because recordings at those distances begin to experience complications from surface waves and crustal multiples (Figure 4.5). The points in-between these distances are then saved with their corresponding coefficient data and coordinates, and then plotted on a map (Figure 2.4) using Generic Mapping Tools (Wessel et al., 2019). Note, the Taup projection assumes a receiver depth of 35km so that a projected datapoint represents energy arriving at the base of the crust rather than the surface.

We also produced another variant of this map that makes use of a cutoff value for the Sv coefficient, where any points that have an assigned value above the cutoff are given a value of 1, while those points that fall below the cutoff are given a value of 0. The resulting map shows a region where the cutoff is satisfied, or as we will refer to it, a "sweet spot" (Figure 3.1).

Multiple sweet spot maps can be summed to show locations that fall within the sweet spots of multiple events (Figure 3.2). In a later section, we produce these summed sweet spot maps with large numbers of events to see locations that could have seen multiple shear-coupled P-wave arrivals.

Currently the cutoff for these maps is defined only in terms of the Sv coefficient, but it is worth noting that this arriving energy is scaled by the magnitude of the source,

so the observability of this energy in the form of converted phases is partially dependent on the noise level at the receiving station as well as the magnitude of the source. With a larger event, or a particularly low noise level, it is theoretically possible to make these observations in areas where the incoming shear energy only has a small component of its energy polarized vertically.

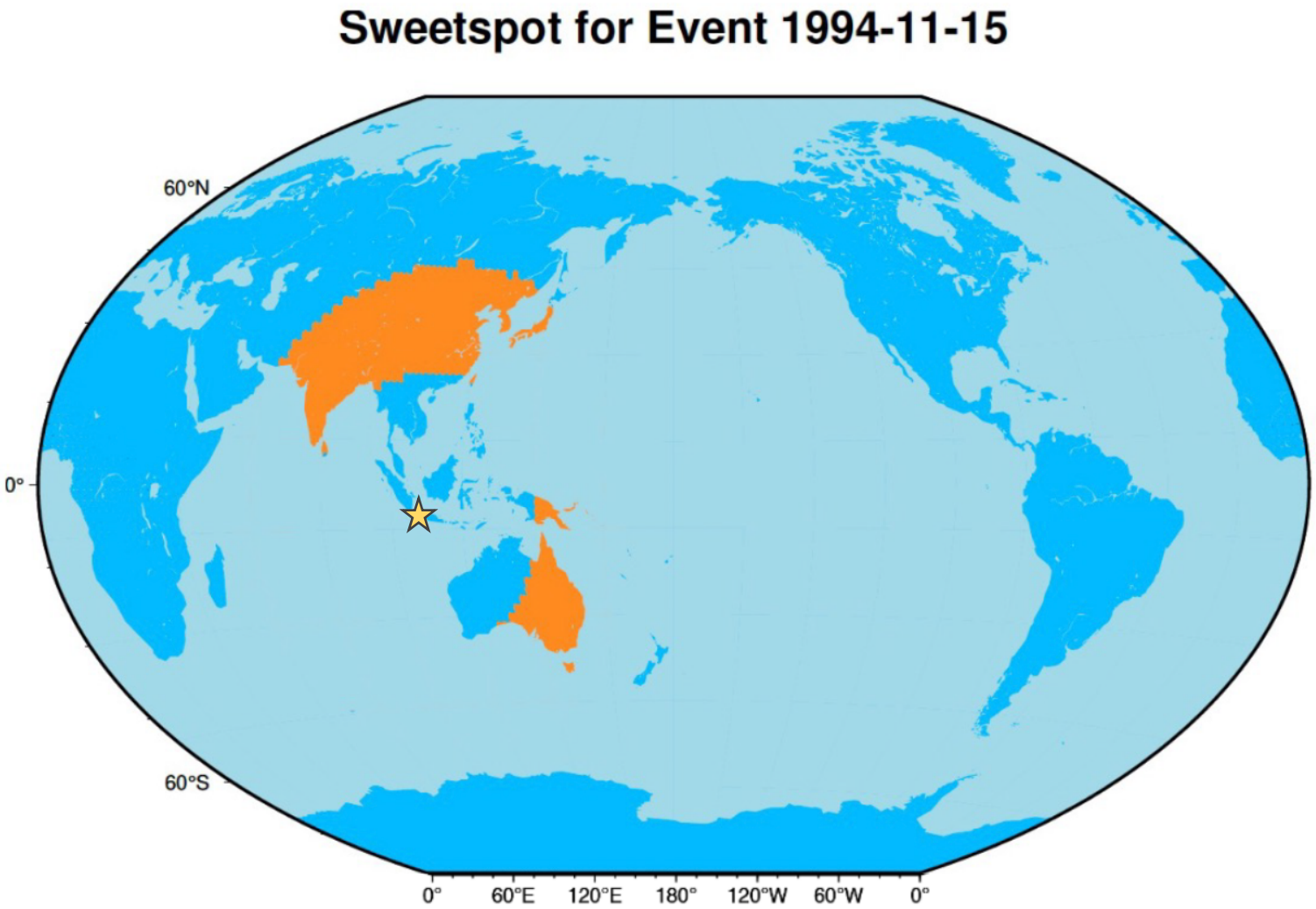

Figure 3.1. Sweet spot map of Event 1994-11-15. Orange denotes the region where incoming mantle S-waves satisfy the controls for shear-coupled P-wave observation while blue represents the region where the controls are not satisfied.

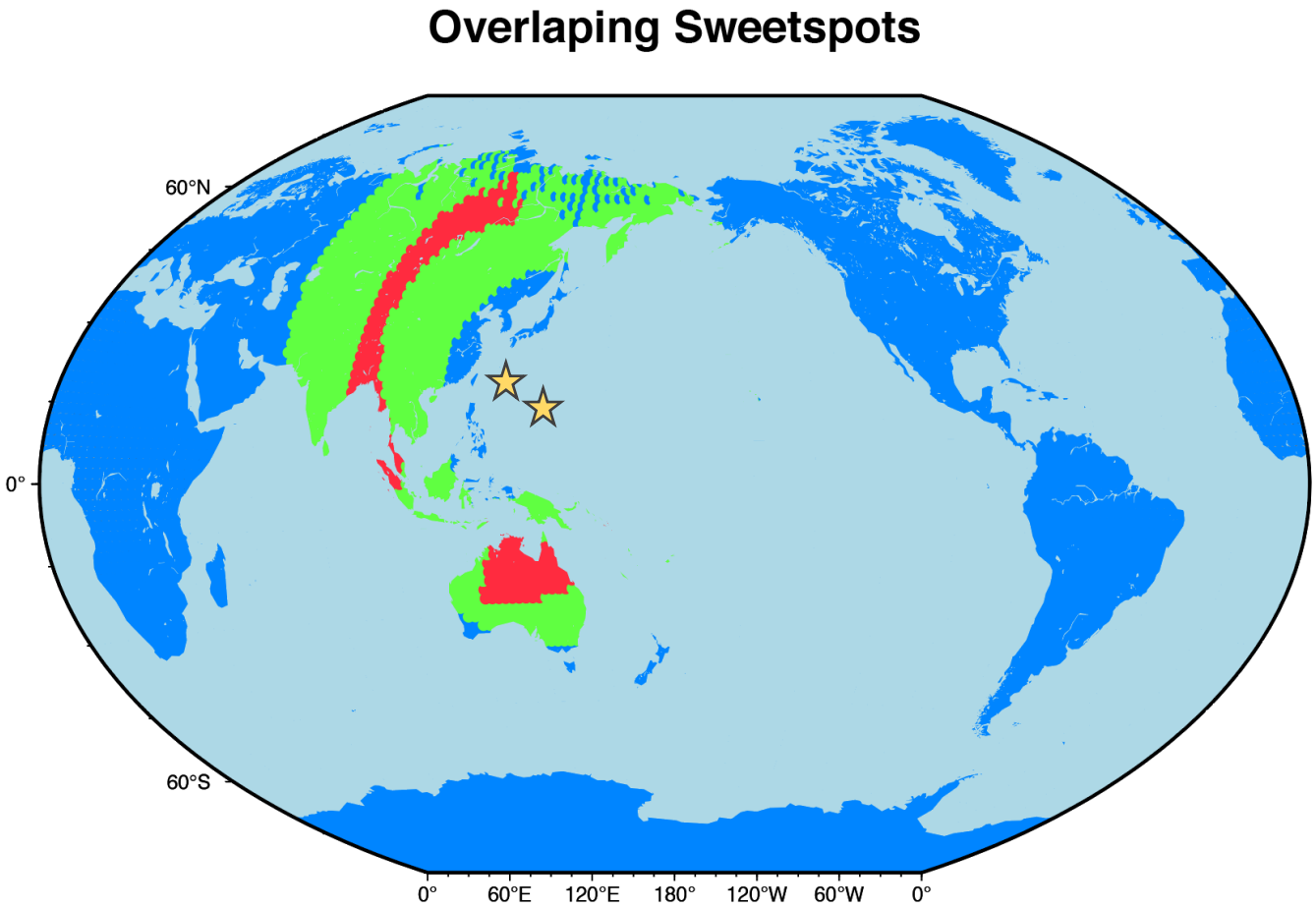

Figure 3.2. Sweet spot map of two overlapping events (Event 2020-06-13T15:51 & Event 2020-06-13T21:08, represented by stars). The surface is green where shear-coupled P-wave controls are satisfied by one event, red where they are satisfied by two event and blue where the controls are not satisfied by either.

Chapter 4:Analysis

3.1 Real Data

While observations of shear-coupled P-waves are limited in the literature, observations have been made by various groups across the globe. Tseng et al. (2009), Owens and Zandt (1997), and Pulliam et al. (2008) were able to make observations of shear-coupled P-waves in China. Gangopadhyay et al. (2007) recorded shear-coupled P-waves arriving at stations in Africa, Liu et al. (2019) observed arrivals in Canada, and Thompson et al. (2019) observed the phase in Australia. To constrain the controls on shear-coupled P-wave observability, we examine these previously recorded sightings.

We collect data from these sources using data collection software called Standing Order for Data (SOD) (Owens et al., 2004). We then sorted out bad data and events with no easily accessible recordings, leaving us with a collection of clean events that, according to literature, should contain shear-coupled P-waves (Table 1). These events are all generally deep and within the distance range that allows for total internal reflection, with the exception of Event 1999-09-15 and Event 1995-05-13, which were recorded at distances greater than the critical distance.

After collecting data from the events in our event list, we began to assess the quality of the shear-coupled P waves recorded for each event. We calculated values for the Sv coefficients of each event station pair using the same methods used to generate our sweet spot maps. While verifying the events, we developed a scale of “yes, no, or

maybe" (1, -1,0) to describe the observability of *SsPmp* for that recording. Plotting Sv coefficients vs observability for the events in our event list shows that observability drops somewhere between Sv coefficients of 0.3 and 0.2 (Figure 4.1).

We then took a close look at one particular event to help verify our synthetics and sweet spot maps. Event 2013-10-01 (Table 1) recorded at station YKW3 was found to be a valid observation of a shear-coupled P-wave (Figure 4.2).

Modeling the event with a synthetic seismogram, we saw a large amplitude *SsPmp* shortly after the main S arrival (Figure 4.3). The synthetics agreed well with the real data in terms of travel time differences between S and *SsPmp* (Figure 4.2 & 10).

We then collected the source parameters from the centroid moment tensor catalog (Dziewonski et al., 1981; Ekström et al., 2012) and created a sweet spot map to display the distribution of Sv coefficients on the globe (Figure 4.4). For this particular event, the Sv coefficient arriving at the base of the crust below station YKW3 is .504.

We then sampled the sweet spot maps along a radial line leaving the event, passing through YKW3, as well as in a circle of equal distance around the source (to sample azimuthal variation in Sv coefficient), using synthetic seismograms (Figure 4.5 & 13). The synthetics calculated for an array of distances showed a sharp drop-off in *SsPmp* amplitude beyond the critical distance of 55 degrees (Figure 4.5). The synthetics calculated at different azimuths sample a range of Sv coefficients (Figure 4.6). As the Sv coefficient decreases, the amplitudes of the *SsPmp* drop.

3.2 Global Sweet Spot Map

After verifying the agreement between our maps and observability, we collected 10 years of moment tensors to make a stacked sweet spot map (Figure 4.7). We select all events, in accordance with our previously defined controls, to have over a 5.5 magnitude, a depth greater than 100 kilometers, and assign a cutoff of 0.3 for the Sv coefficient.

Our global sweet spot map indicates that between 2000 and 2009 there were a large number of events that produced potentially observable shear-coupled P-waves in several locations (Figure 4.7). The regions with the greatest potential for observing shear-coupled P-waves are Australia, Papua New Guinea, East Asia, and parts of Antarctica, though the potential to make an observation exists across most of the globe. In locations with a high number of predicted arrivals (colored yellow, red and pink in Figure 4.7), one could expect 10 or more events per year to satisfy all of the controls we have defined for observable shear-coupled P-waves, meaning that, on average, temporary deployments with lifespans around 2 years could expect to see more than 20 clear shear-coupled P-wave arrivals. It is possible to make observations across most of the remaining globe, but with lower reliability (black, blue, and green in Figure 4.7.). Making observations in these areas may only be feasible for long running stations, like those in the Global Seismographic Network (1988). Gangopadhyay et al. (2009) observed potential shear-coupled P-waves in Namibia and Zambia, though these events did not satisfy our distance control. In the Northwest Territories, Canada, the annual expected arrivals is only 3 or 4 per year, but studies like Liu et al. (2019) were still able to collect a data set due to the long deployment of the recording station, YKW3.

3.3 Verifying Global Sweet Spot Map

After generating our global sweet spot map and assessing the locations on the earth where shear-coupled P-waves should have the highest rate of occurrence, we narrow our search to Australia. According to our global sweet spot map (Figure 4.7), we should see approximately 22 clear shear-coupled P-waves recorded in central Australia for any given year. To test the observability of shear-coupled P-waves in central Australia, we take a two-pronged approach: utilizing previous findings from the literature, as well as data collection and interpretation.

We also investigate the findings of Thompson et al.'s (2019) study on Virtual Deep Seismic Sounding in greater detail to assess the feasibility of finding and utilizing shear-coupled P-waves within central Australia. Additionally, using insights from Thompson et al (2019), we select a seismic station in central Australia (WRAB) and collect a single year's worth of data to assess for shear-coupled P-wave observability.

3.4 Prior Findings

Literature review shows that observations of shear-coupled P-waves are common in Australia. Several studies, such as Zielhuis & Hilst (1996), Clitheroe et al. (2000) and Thompson et al. (2019) have made use of shear-coupled P-waves for the purpose of better understanding the lithosphere of Australia. Specifically, studies like Thompson et al.'s (2019) investigation of virtual deep seismic sounding make use of multiple observations of shear-coupled P-waves to assess crustal structure beneath central Australia. Data from this study was collected at both a long standing permanent station (WRAB) and across a temporary array deployed along a north-south tract

spanning central Australia (BILBY). For the purposes of our study, we will focus on Thompson et al.'s (2019) findings at station WRAB, but we also note that this work, as well as other studies like Clitheroe et al.'s (2000) work with the SKIPPY array, suggests that observing shear-coupled P-waves on temporarily deployed arrays is possible in areas with a high value of expected annual shear-coupled P-wave arrivals from our global sweet spot map (Figure 4.7).

Using the multiply reflected nature of shear-coupled P-waves, Thompson et al. (2019) was able to calculate the depth of the Moho beneath WRAB using a large number of events that produced observable shear-coupled P-wave arrivals. Thompson et al.'s results show that events that originate from the north, in Java subduction zone, produce waveforms with smaller delay between the main S phase and the following *SsPmp* phase when compared with events that originate to the east, in the Tonga-Fiji subduction zone.

After collecting data from a large number of events, Thompson et al. (2019) were able to use the arrival times of shear-coupled P-waves, in conjunction with an H-Vp inversion technique, to find an average crustal thickness over the areas that these phases sampled.

Ultimately, these results show that shear-coupled P-waves can be observed on the waveforms of many events recorded within Australia, but they also provide a better understanding of the crust sampled by shear-coupled P-waves originating from two different subduction zones. To the north, inversion results indicated that the crust has an average thickness of 40.8 kilometers, while to the east, inversion results indicate that

the crust is slightly thicker, with a thickness of 41.6 kilometers. In the next section we will use what we've learned about the crust surrounding station WRAB to assist in the identification of shear-coupled P-waves produced during the year 2020, as well as seeing if our data agrees with the crustal structure proposed by Thompson et al. (2019).

3.5 Data and Synthetics

After completing our literature review, we decided to gather data from the seismic station WRAB to assess the accuracy of the predictions made by our global sweet spot map (Figure 4.7). In order to verify the predictions made by our global sweet spot map (Figure 4.7), we seek observations of shear-coupled P-waves at WRAB during the year 2020. We note that our decision to collect data from the year 2020 was motivated by a global decrease in noise as a result of the COVID-19 pandemic (Lecocq et al., 2020).

Using SOD (Owens et al., 2004), we collect data from 32 different events listed in Table 2. These events all satisfy the conditions set by our previously defined depth, magnitude, and distance controls. All events collected are greater than 100km in depth, originate within a range of epicentral distances between 30-60 degrees from station WRAB (slightly larger than our previously defined range in order to potentially observe the post-critical regime), and have magnitudes greater than 5.5.

While distance, depth, and magnitude are accounted for by our event collection process, assessment of the sweet spots for these events is not complete without considering Sv polarization. For this reason, we plot all of our events using our sweet spot calculation method and produce a sweet spot map for our dataset (Figure 4.8). We

can see that, for this dataset, the greatest overlap for sweet spots happens to fall in the regions immediately surrounding station WRAB. The number of predicted arrivals in our new sweet spot map (Figure 4.8) agrees with our global sweet spot map (Figure 4.7), predicting that we should see around 22 shear-coupled P-wave arrivals in this data.

Additionally, in a later section we compare our findings to those of Thompson et al. (2019), which makes average crustal thickness determinations using multiply reflected shear-coupled P-waves. These averages encompass the areas where the crust is sampled by shear-coupled P-waves. For this reason, we have included a map with the pierce points for the various phases that we discuss in this paper (Figure 4.9).

Using a combination of manual observation and comparison with synthetic seismograms, we log the observability of shear-coupled P-waves for each event in Table 2 to confirm that the number of arrivals implied by our new sweet spot map (Figure 4.8) is accurate. Our determination for the observability of each event is listed in Table 2, under the observation column, where 1 represents an observable shear-coupled P-wave and -1 represents the absence of a shear-coupled P-wave. For events in which we had low confidence but could potentially be shear-coupled P-waves, we assign an observability score of 0.

In total, our 2020 data set includes 21 events with confirmed shear-coupled P-waves, as well as 7 events that are unconfirmed, and 4 events that have a confirmed absence of shear-coupled P-waves. These values agree with both our global sweet spot map (Figure 4.7) and the sweet spot map representing the events of Table 2 (Figure 4.8).

After completing our observability determinations, we can again plot the Sv coefficient vs observability (Figure 4.10).

3.6 Event 2020-06-13

Event 2020-06-13 originated to the north of WRAB, in the Java subduction zone, had a source depth of 165 kilometers, an epicentral distance of 48.8 degrees, a magnitude of 6.6, and an Sv Coefficient of 0.108. The waveform recorded for this event at WRAB is shown in Figure 4.11. The main S-wave arrives at approximately 919 seconds as an out-of-phase arrival on the radial and vertical traces. Following the S-wave, we see an in-phase arrival approximately 9 seconds later, which we identify as *SsPmp*. Additionally, 6 seconds prior to the main S-wave arrival, we see a smaller in-phase arrival that we identify as *Sp*. According to our predictions (based off our Sv cutoff of 0.3), these phases should be small or even unobservable, but despite this we see both *SsPmp* and associated multiples like *SsPmpPmp* and *SsPmpPmpPmp*. To explain this contradictory appearance, we note that the magnitude of this event is relatively high for our dataset (6.6), and also that the noise level at the receiver is low, especially considering the data was collected during the year 2020 when anthropogenic noise was considerably reduced (Lecocq et al., 2020). We also see these unexpected arrivals on other low Sv events (Table 2, Figure 4.10), and in these cases we note a either a large magnitude or a small epicentral distance.

To further verify our findings within this event, we generate a set of synthetic seismograms, using the same source moment tensor, depth, distance, and azimuth (Figure 4.12). We also note the custom velocity model that we use in the generation of

this synthetic. Thompson et al (2019) found that, for events originating to the north of WRAB, the sampled crust has an average thickness of 40.8 kilometers, a crustal P-wave velocity of 6.5 km/s, and a crustal S-wave velocity of 3.75 km/s. The values for this crust were pasted on top of the ak135 velocity model and used in our synthetic calculation. Comparing the waveforms of both the synthetics and the real data, we see a loose agreement in phase arrival times and strong agreement in character. The S-wave of our synthetic appears slightly before the S-wave of our original data, at about 918 seconds. Also present within the synthetics, we see in-phase arrivals at about 6 seconds prior to the direct S-wave (*Sp*), 9 seconds after the direct S-wave (*SsPmp*), which agree roughly with our real data. 21 seconds after the main S-wave, we see another in-phase arrival, *SsPmpPmpPmp*, though for these phases the corresponding phase within the real data arrives later. Finally, about 14 seconds after the direct S-wave there is an out-of-phase arrival where we expect *SsPmpPmp.* Using Taup (Crotwell et al, 1999) we confirm that this phase is not an interfering global phase or depth phase, and is most likely the multiply converted phase *SpPmpPms*.

Ultimately, while similar waveforms are present, the differences in relative arrival times between our real data and the synthetics seem to indicate that our crustal model has a smaller thickness than the real-world crust sampled during this event. Other events observed from the same source region have relative arrival times that agree with the data from event 2020-06-13.

3.7 Event 2020-11-11

Another event that we investigated was event 2020-11-11. This event originated in the Tonga-Fiji subduction zone to the east of station WRAB. With a source depth of 417 kilometers, an epicentral distance of 45.1 degrees, a magnitude of 6.0, and an Sv coefficient of 0.714. This event, in contrast to event 2020-06-13, satisfies all of our previously defined controls, including the Sv coefficient. The vertical and radial components for this event are shown in Figure 4.13. As expected, we see clear shear-coupled P-wave arrivals.

Within our waveforms, we see our main S-wave arrival at approximately 822 seconds following the origin time of the event. Before the S-wave, we also see an in-phase arrival we identify as *Sp* (6 seconds prior to S). Following the S-wave by 7 seconds, we see a large in-phase arrival we identify as *SsPmp*, followed later by *SsPmpPmpPmp* (23 seconds after S). We also note the presence of an out-of-phase arrival, approximately 16 seconds after the direct S-wave. This phase is likely the multiply converted phase *SpPmpPms* observed in the synthetic of event 2020-06-13 (Figure 4.12).

Once again, we compute synthetic seismograms in accordance with the findings of Thompson et al. (2019), using a crustal model with a thickness of 41.6 km, Vp of 6.5 km/s, and Vs of 3.75 km/s, to assist in the verification process (Figure 4.14). We find that, as compared to the synthetics generated for event 2020-06-13, these synthetics agree much better with the waveforms of our real data in terms of character and arrival times. The main S-wave arrives at nearly the same time as the original data's main S-

wave arrival (823 seconds). The shear-coupled P-wave arrivals also match the arrivals within the original data, with an *Sp* phase arriving at approximately 6 seconds before the direct S-wave, *SsPmp* arriving at 8 seconds after, and finally *SsPmpPmpPmp* 21 seconds after *S*. Similar to our real data, we observe the presence of *SpPmpPms* approximately 16 seconds after the direct S-wave arrival. These results, as well as the relative arrival times observed in other events originating from the East, imply that the model Thompson et al. (2019) calculated for the crust lying to the east of station WRAB is representative of the real earth structure, while the model calculated for the north is likely thinner than the real crust.

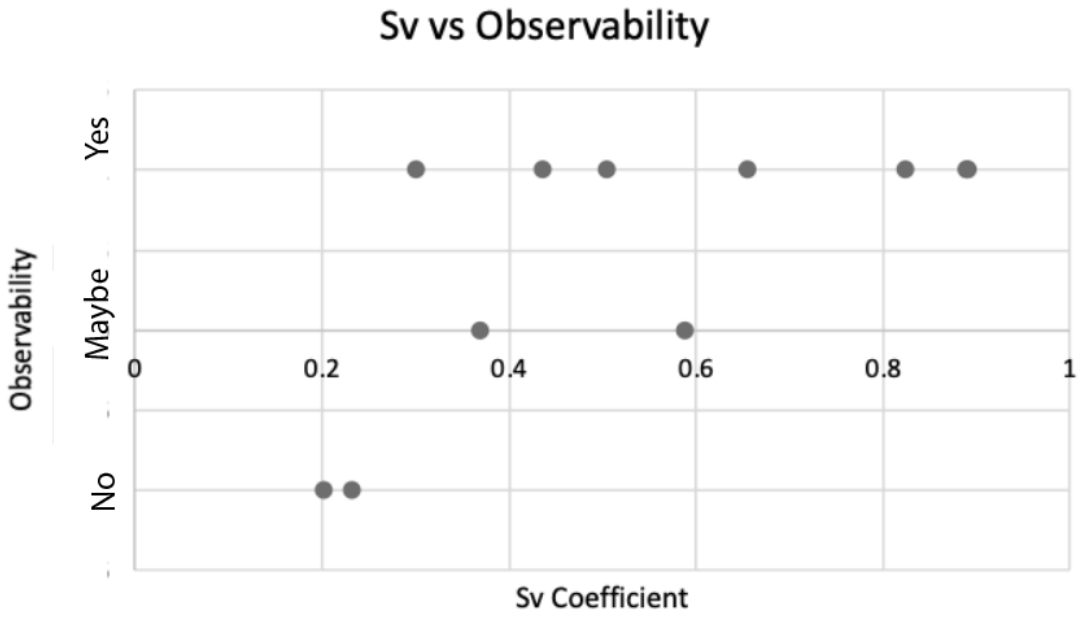

Figure 4.1. Plot of Sv coefficients vs observability for all events in Table 1.

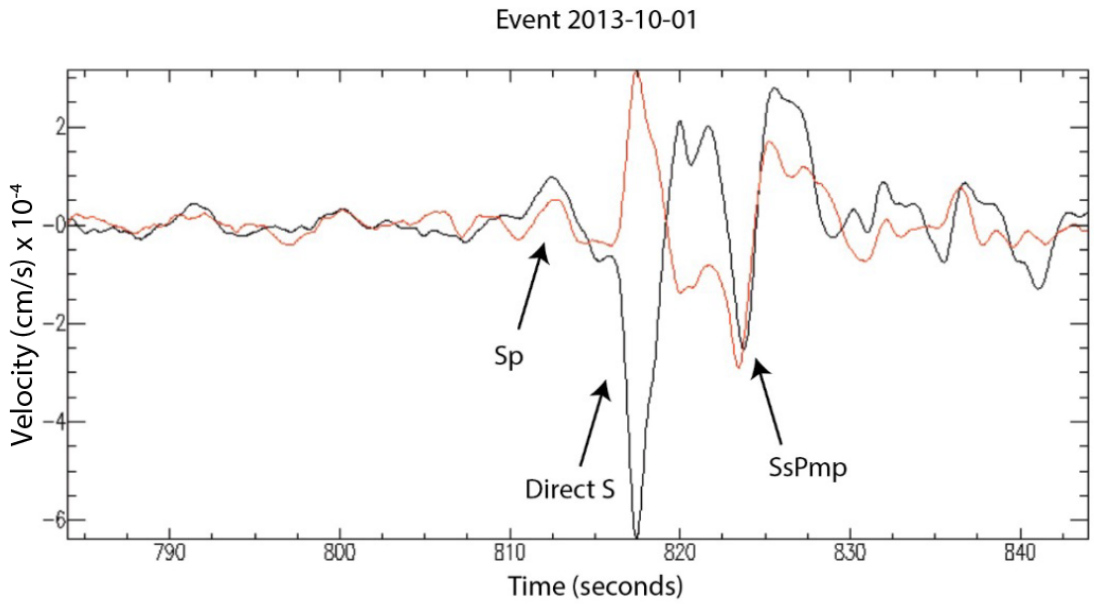

Figure 4.2. Event 2013-10-01 recorded at station YKW3. The radial (black) and vertical (red) components are out of phase at approximately 817s (indicating a shear wave arrival) and in phase at 823s (indicating a P-wave arrival). The P arrival at 823 follows the main S arrival by about 6 seconds, which is in the range of arrival times for SsPmp.

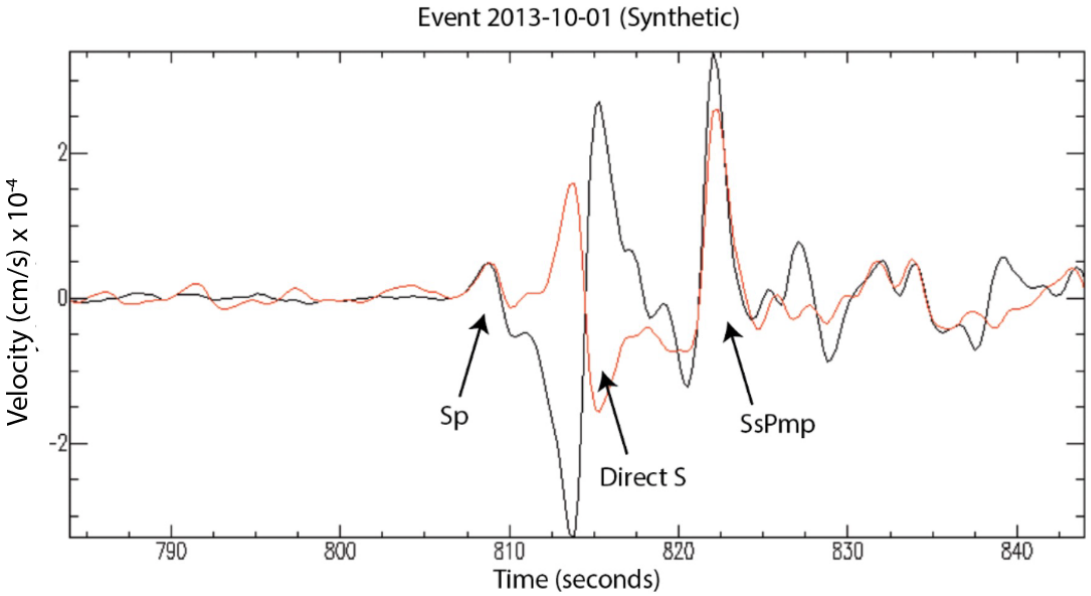

Figure 4.3. Synthetic seismogram produced using the source moment tensor and depth of event 2013-10-01 using the ak135 velocity model (Kennett et al., 1995). A large SsPmp arrival can be seen at approximately 823.5 seconds, about 8 seconds after the main S arrival. This synthetic produces similar arrivals to the real data recorded at YKW3.

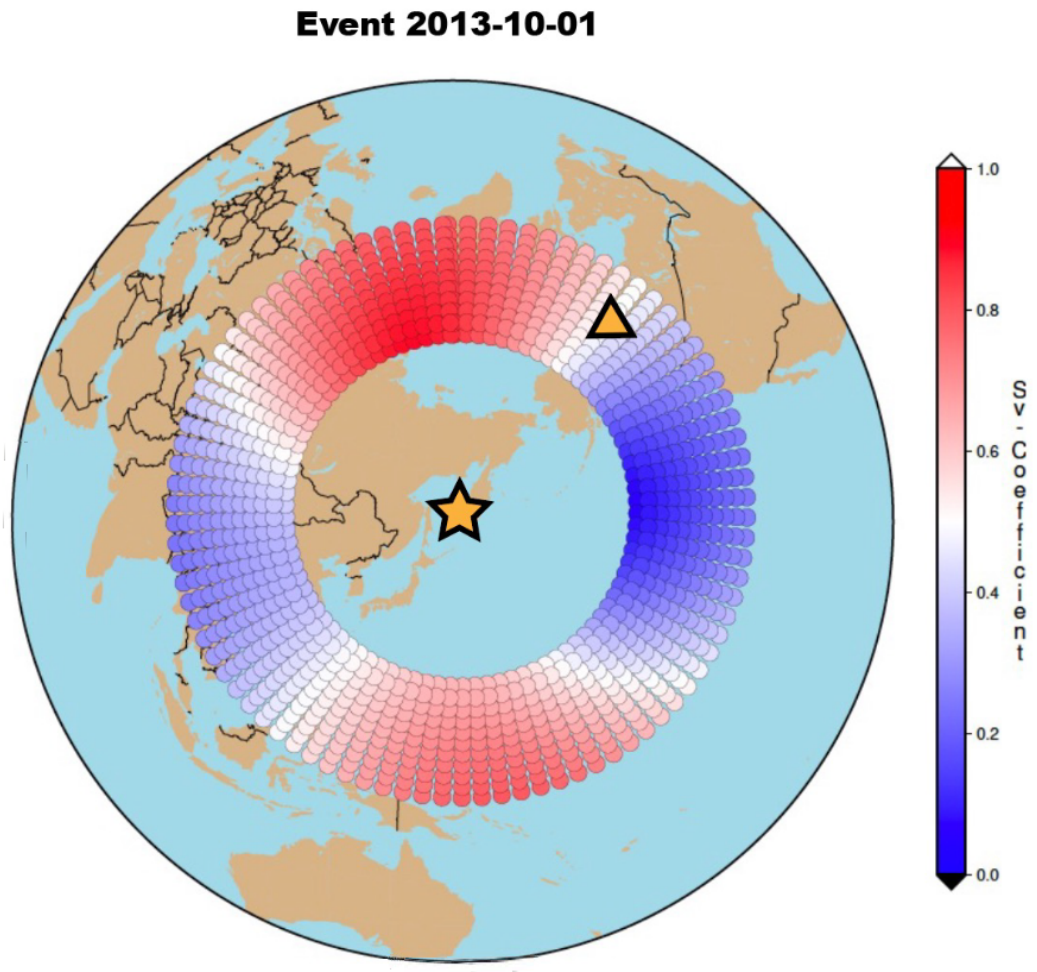

Figure 4.4. Individual sweet spot map for event 2013-10-01. Station YKW3 is denoted by a triangle. The value of the Sv coefficient at this location is .504.

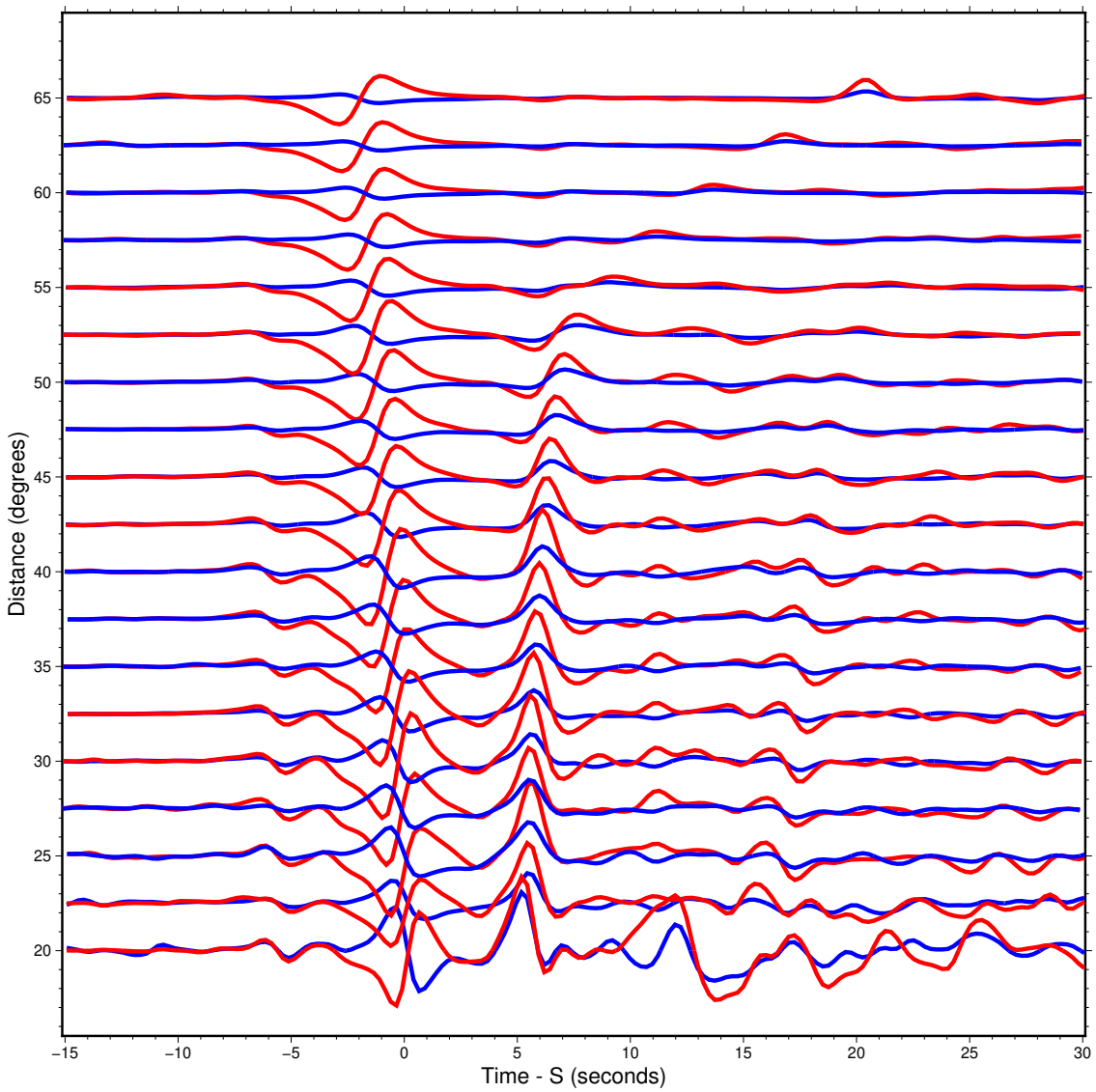

Figure 4.5. A record section of synthetics seismograms calculated for event 2013-10-01. The blue represents vertical motion, and red represents radial motion. As distance increases beyond 55 degrees the critical distance is passed and the amplitude of the second pulse (SsPmp) drops off. At these distances, P-waves are able to escape into the mantle, turn, and reenter the crust to be recorded following the small amplitude reflected SsPmp. For interpretation, all traces are normalized to the S-wave arrival. This allows us to see the amplitude of phases in the S-coda relative to direct S arrival of a trace.

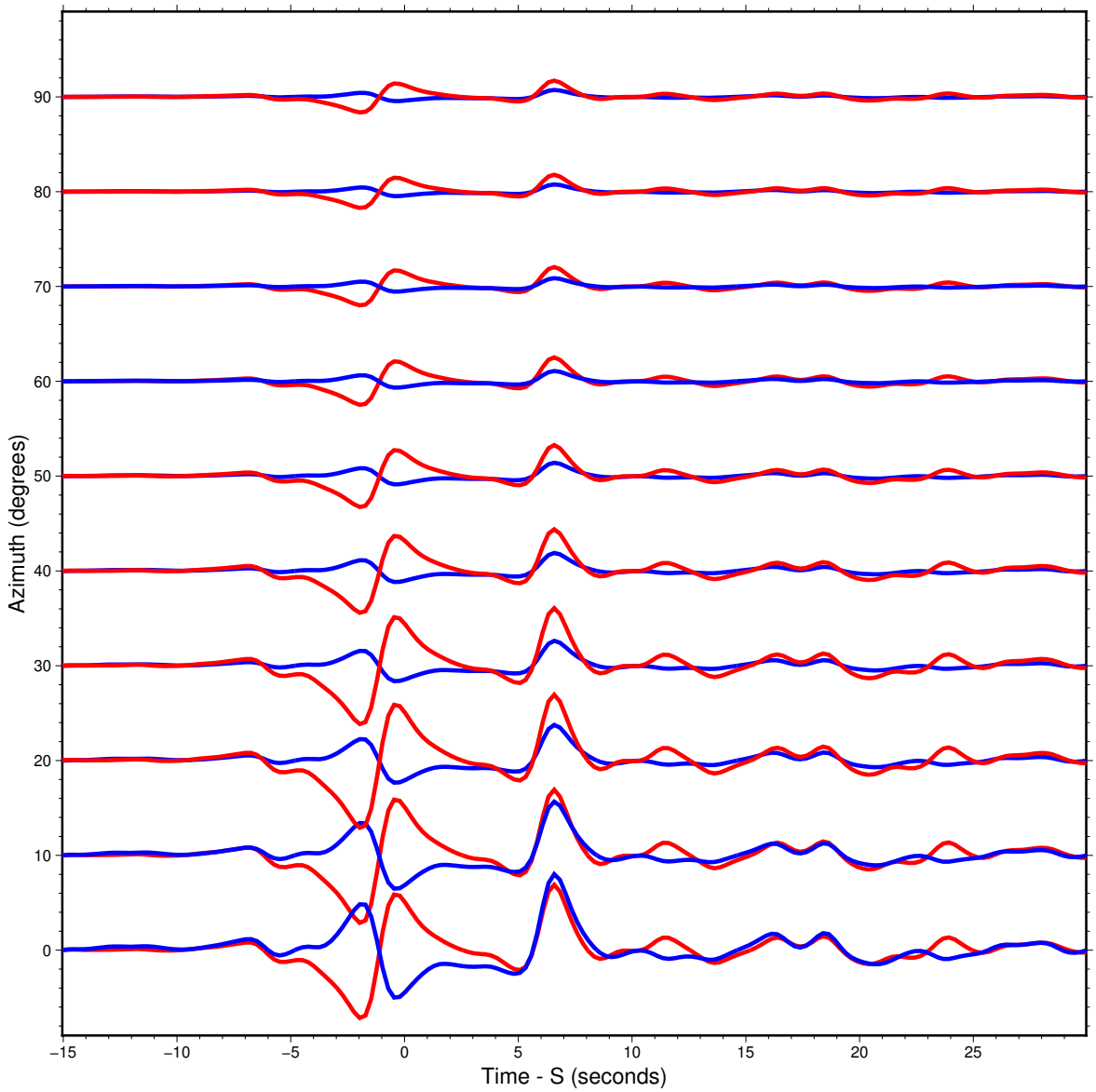

Figure 4.6. A record section of synthetic seismograms calculated for event 2013-10-01. 0 on the y-axis represents north and 90 represents east. Once again, blue represents vertical motion, and red represents radial motion.. As the synthetics pass through azimuths that sample lower Sv coefficients, the amplitude of those arrivals decreases. As opposed to the traces in Figure 4.5, all traces on this record section represent ground motion without any scaling factor to show true differences in amplitude between traces.

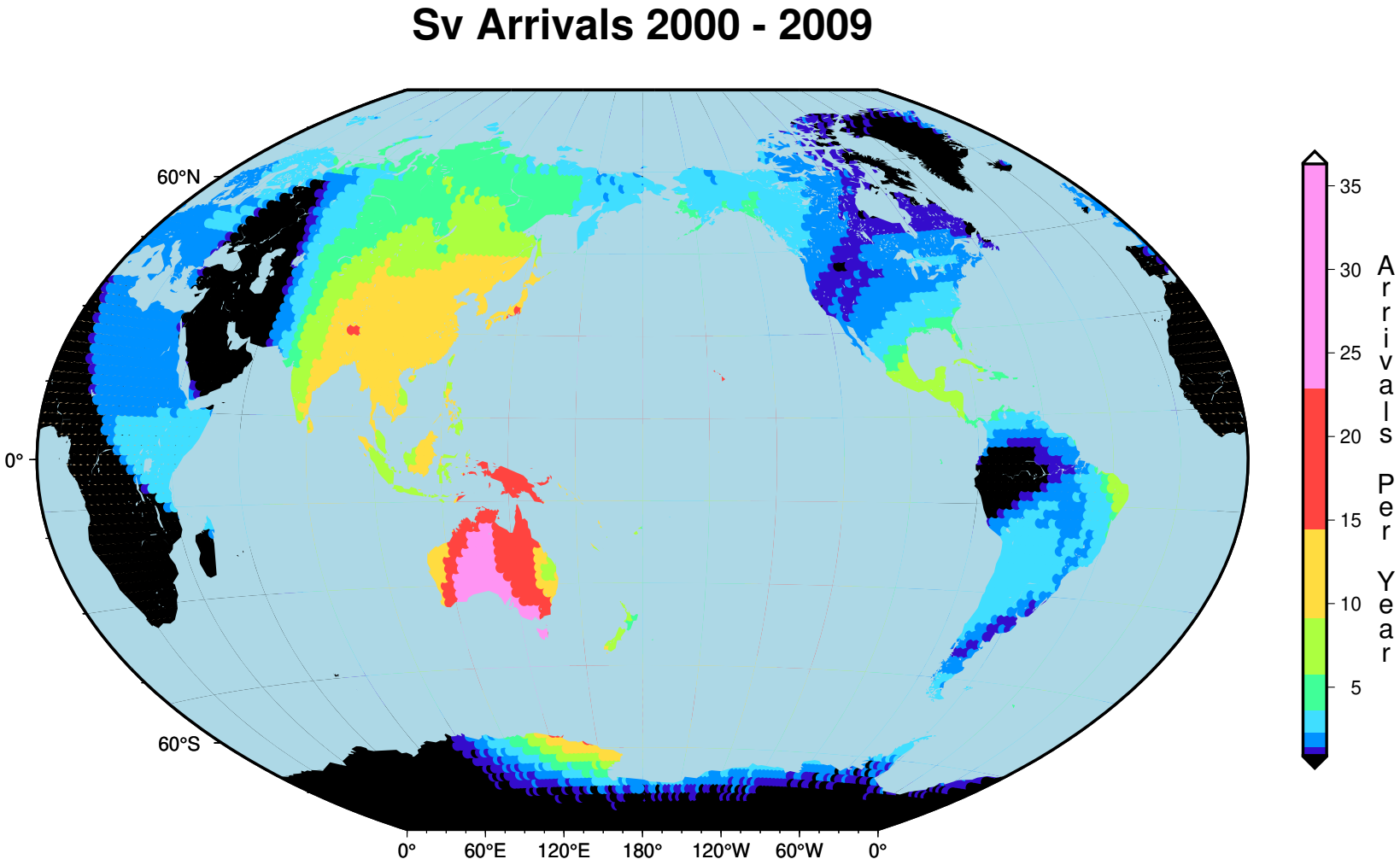

Figure 4.7) Global sweet spot map generated using 10 years' worth of data. All event sources are greater than 100 kilometers in depth and greater than 5.5 in magnitude. The selected cutoff value for Sv is 0.3, and the distance window for total internal reflection is from 32 degrees to 55 degrees. The values on the color bar represent the number of events that could produce a shear-coupled P-wave at a location on average each year.

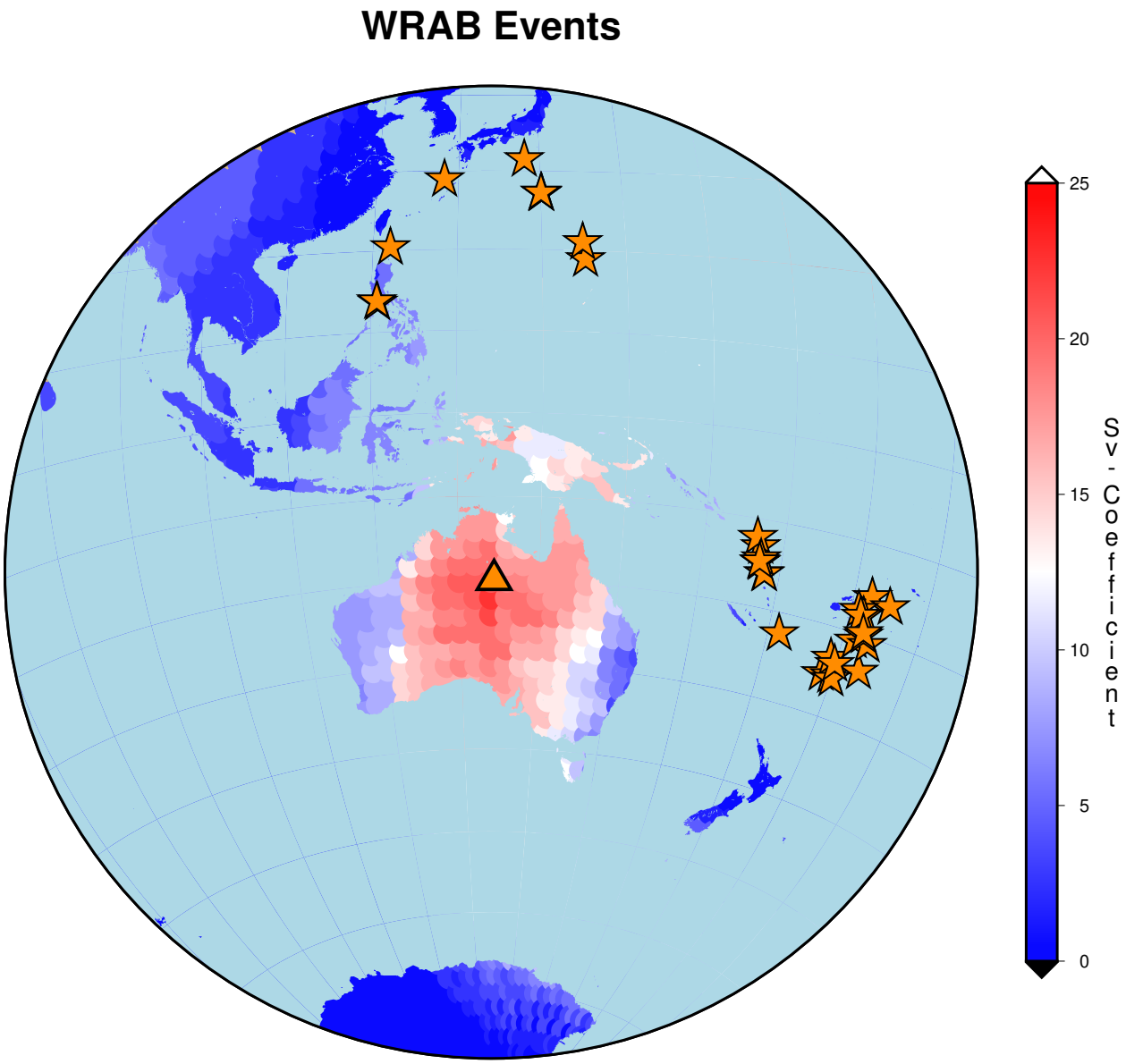

Figure 4.8. Sweet spot map depicting the events collected for station WRAB during 2020. All events are compliant with our previously defined controls with source depths greater than 100 kilometers, magnitudes greater than 5.5. Sweetspots are calculated with distance windows of 32 to 55 degrees epicentral distance and Sv cutoffs of 0.3. The color bar indicates the number of overlapping sweet spots in a location. Station WRAB is depicted as a yellow triangle (at 19.9 S, 134.4 E).

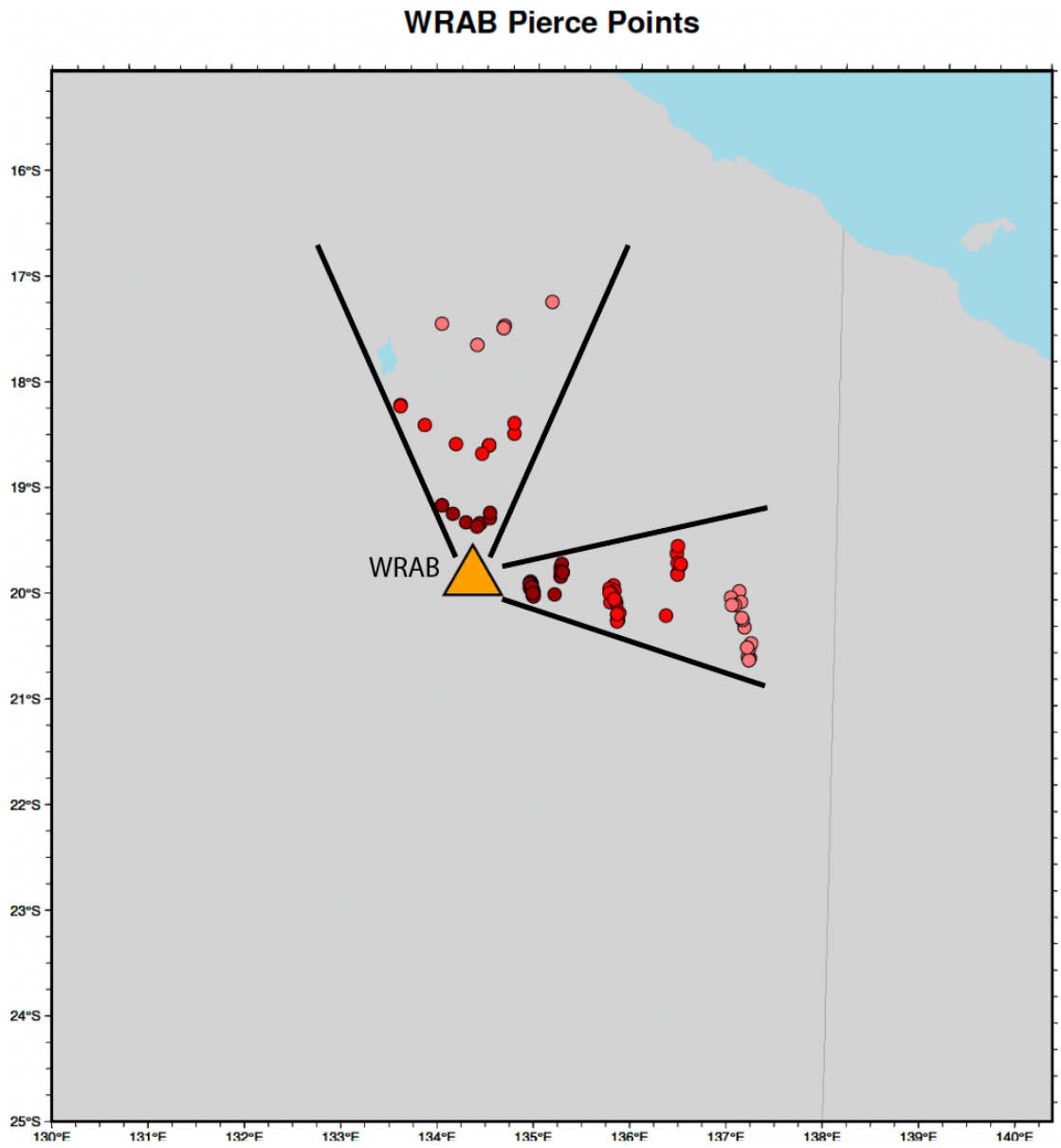

Figure 4.9. Pierce points associated with the events collected in Table 2. Each point denotes where a particular phase enters the crust. Sp (dark red), SsPmp (red), SsPmpPmp (light red). We note the limited azimuthal range sampled by these events. We also note that due to mantle triplication, some events produce SsPmpPmp phases that pierce the crust much further from the recording station.

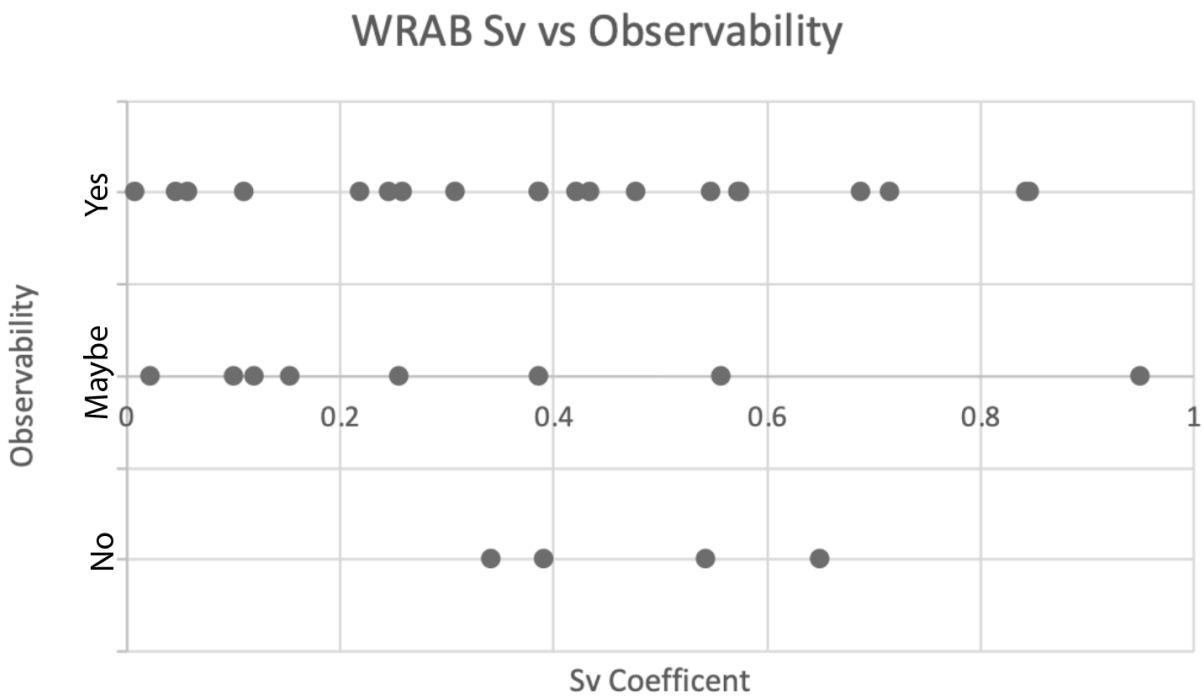

Figure 4.10. Plot of Sv coefficients vs observability for all events in Table 2.

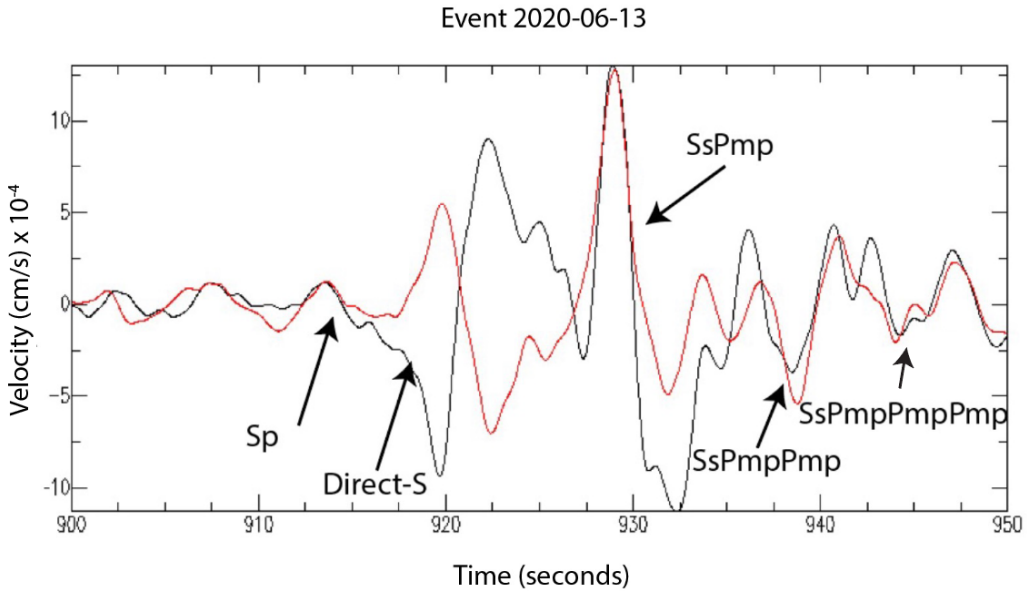

Figure 4.11. Real data from event 2020-06-13 recorded at station WRAB. The radial (black) and vertical (red) components are out of phase at approximately 919 seconds (indicating a shear wave arrival). Several in-phase arrivals (P-waves) are shown in this data: Sp (6 seconds before S), SsPmp (9 seconds after S), SsPmpPmp (approximately 19 seconds after S) and SsPmpPmpPmp (24 seconds after S)

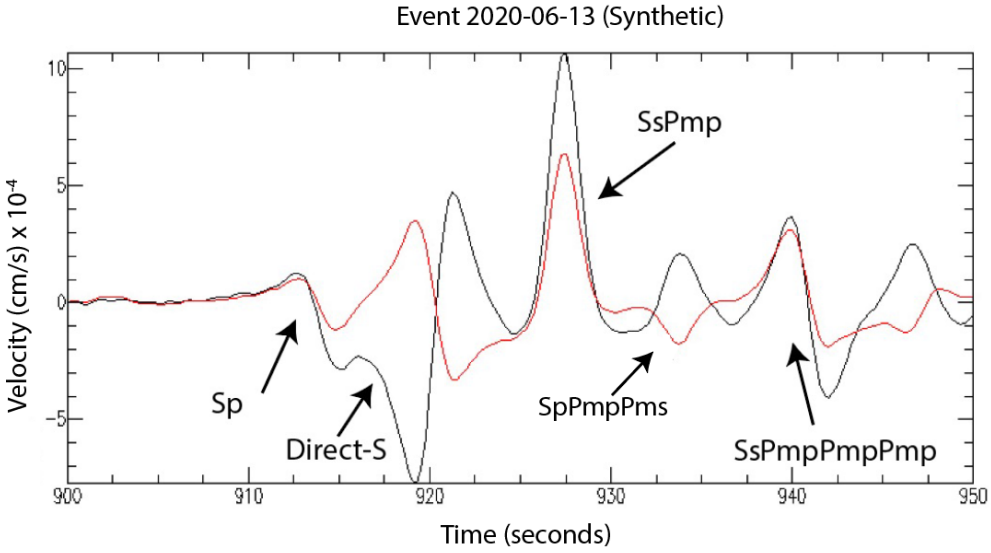

Figure 4.12. Synthetic seismograms generated using the source of event 2020-06-13 recorded at station WRAB on the radial (black) and vertical (red) components. The direct S-wave arrives at approximately 918 seconds. S is preceded by Sp (6 seconds), and followed by SsPmp and SsPmpPmpPmp (9 seconds and 21 seconds after S respectively). We also note the out-of-phase arrival roughly 14 seconds after the direct S-wave which is likely the multiply converted phase SpPmpPms.

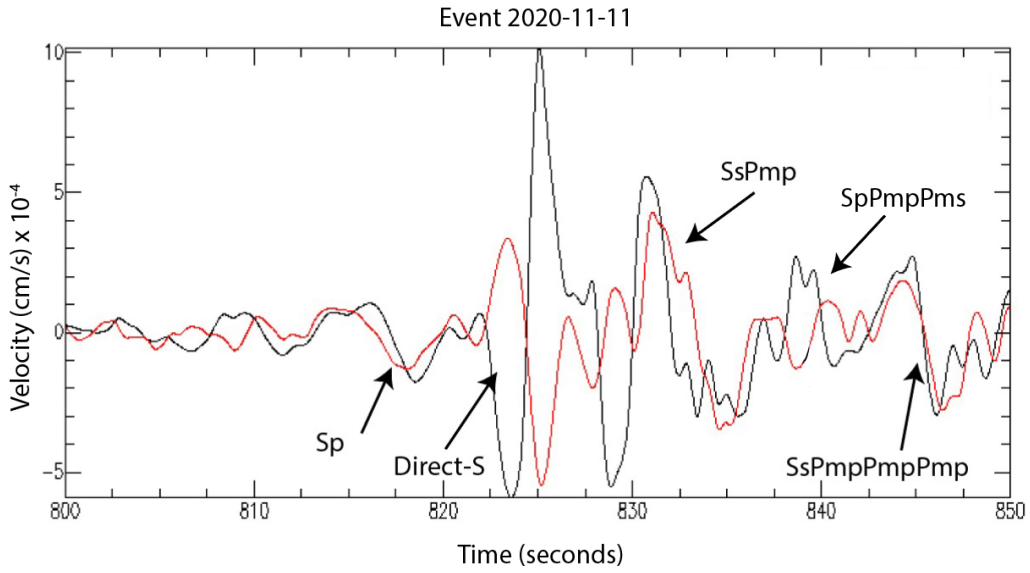

Figure 4.13. Real data recorded at station WRAB on 11/11/20 on the radial (black) and vertical (red) components. The direct S-wave arrives at approximately 822 seconds. Sp precedes the direct S-wave by about 6 seconds, while SsPmp and SsPmpPmpPmp follow the direct S-wave by 7.5 and 21 seconds respectively. Aproximately 16 seconds following the S-wave there is an out-of-phase arrival that we suspect is the phase SpPmpPms.

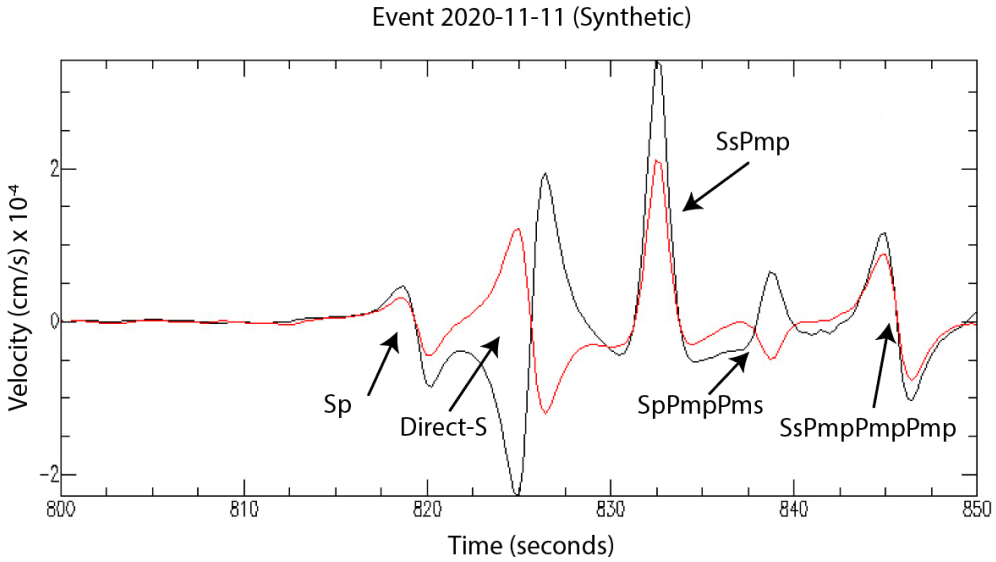

Figure 4.14. Synthetic seismograms generated using the source of event 2020-11-11 recorded at station WRAB on the radial (black) and vertical (red) components. The direct S-wave arrives at approximately 823 seconds. Similar to the real data, Sp precedes the direct S-wave by about 6 seconds, while SsPmp and SsPmpPmpPmp follow the direct S-wave by 7.5 and 21 seconds respectively. Once again, 16 seconds following the main S-wave arrival we see an out-of-phase arrival (SpPmpPms).

Table 3.1. Reported shear-coupled P-wave observations.

Station	Event	O-time	Latitude	Longitude	Depth (km)	Distance (degrees)	Mw	Sv	Observable
TSUM	1999-09-15	3:01:24	-20.93	-67.28	217.5	78.91	6.4	0.587	0
LSZ	1995-05-13	21:00:54	-5.22	108.92	581.9	79.96	5.8	0.232	-1
BJT	1994-09-28	16:39:52	-5.7	110.3	652.7	45.88	6.6	0.824	0
BJT	1994-11-15	20:18:11	-5.5	110.1	570.7	45.71	6.5	0.891	0
YKW3	2004-07-08	10:30:47	47.1	151.7	132.8	51.13	6.3	0.3	1
YKW3	2009-12-10	2:30:52	53.4	152.7	655.7	45.77	6.3	0.436	1
YKW3	2013-10-01	3:38:21	53.2	152.8	585.5	45.77	6.7	0.504	1
YKW3	2004-06-10	15:19:56	55.7	160.3	190.1	41.1	6.8	0.201	0
WNDO	1992-03-27	20:33:07	48.01	147.07	450.6	43.35	5.6	0.889	1
H1230	2005-02-05	12:23:18	5.32	123.34	530.6	44.12	7.1	0.369	-1
H1230	2004-11-07	2:02:27	47.93	144.49	493	47.73	6.1	0.655	0

Table 3.2. Events collected for the year 2020. All events comply with our previously defined depth, distance, and magnitude controls.

Event Date	Origin Time (GMT)	Latitiude	Longitude	Depth (km)	Distance (degrees)	Magnitude	Sv	Observable
2020-01-31	13:53.31	-25.3	178.4	574.8	40.8	5.7	0.307	1
2020-03-18	03:13.45	-13.1	167	176	31.9	6.1	0.841	1
2020-03-23	20:33.39	-25.2	179.7	506.1	42	5.5	0.419	1
2020-04-08	10:02.32	-15.7	-177.5	422	45.8	5.5	0.546	1
2020-04-10	16:44.56	20.4	122.1	160	41.9	5.9	0.256	1
2020-04-18	08:25.37	27.1	140.1	453	47.1	6.6	0.385	0
2020-04-18	09:24.18	27.2	140	473.6	47.1	5.7	0.385	1
2020-05-12	22:41.12	-12	166.6	107	31.9	6.6	0.948	0
2020-05-16	03:15.44	-16	168	170.5	32.1	5.9	0.254	0
2020-05-31	23:25.43	-23.9	-176.6	128	45.4	5.8	0.39	-1
2020-06-10	04:29.20	-23.4	179.2	541.3	41.7	5.9	0.385	1
2020-06-13	15:51.24	28.8	128.2	165	48.8	6.6	0.108	1
2020-06-13	21:08.30	18.9	145.1	622	40	6.2	0.844	1
2020-06-17	06:24.18	-16.1	-174.9	281.5	48.1	5.6	0.571	1
2020-06-19	10:07.56	-17.4	-178.9	544	44.2	5.6	0.341	-1
2020-07-05	18:50.01	-14.9	167.3	115	31.8	5.8	0.218	1
2020-07-06	12:58.04	21	144.8	125	41.9	5.5	0.648	-1
2020-07-06	18:19.09	31.5	138.1	388.5	51.2	5.7	0.541	-1
2020-07-21	20:56.25	-20.8	-178.6	605.2	43.9	6	0.055	1
2020-08-05	12:05.36	-16	168	181.8	32.2	6.4	0.045	1
2020-09-12	02:37.29	-17.8	-178	559.6	44.9	5.6	0.02	0
2020-09-16	08:44.28	-22.3	171.5	102	34.7	5.7	0.006	1
2020-10-04	18:16.53	13.6	120.7	121	35.9	5.6	0.152	0

2020-10-06	10:11.46	-17.9	-178.4	633	44.5	5.9	0.433	1
2020-10-22	08:24.07	-20.8	-176.6	244	45.8	5.8	0.476	1
2020-10-23	07:04.30	-25.6	-179.9	454	42.3	6.1	0.099	1
2020-10-28	14:12.56	-14.4	167.4	180	32	5.8	0.687	1
2020-11-03	08:18.56	-19.9	-177.4	388	45.1	5.7	0.574	1
2020-11-11	00:48.44	-19.7	-177.5	417	45.1	6	0.714	1
2020-11-29	09:01.35	-14.7	167.2	108.5	31.7	5.6	0.556	0
2020-12-14	01:57.10	-23.9	179.8	525.5	42.2	5.6	0.118	0
2020-12-24	23:43.41	13.8	120.6	109	36.1	6.3	0.244	1

Chapter 5: Discussion

The results of our data collection at WRAB for the year 2020 agree with the number of arrivals predicted by both our global sweet spot map (Figure 4.7) and our sweet spot map calculated for the events of Table 2 (Figure 4.8). This agreement supports the validity of our controls for depth, distance, magnitude, and S-wave polarization.

We do note a discrepancy revealed in our data by comparison of the Sv coefficient and observability (Figure 4.10). While the total number of observed shear-coupled P-waves within our data agrees between our sweet spot maps, when we calculate the Sv coefficient for each event and plot those values against the observability scores assigned for those events, the resulting plot (Figure 4.10) indicates that our previously determined cut-off (0.3 Sv coefficient) may not be a reliable predictor of shear-coupled P-wave observability, and that the Sv coefficient is not an absolute control on observability. Many events with low Sv coefficients seemed to produce shear-coupled P-waves that are clearly observable. Also, four events with Sv coefficients greater than 0.3, that comply with the rest of our controls, did not produce observable shear-coupled P-waves. These results indicate that, in spite of low Sv coefficients, events can still produce observable shear-coupled P-waves, provided the incoming mantle S-wave is not entirely horizontally polarized and sufficient is energy converted into P-waves, allowing the phases to arrive above noise level. In the case of

event 2020-06-13, we believe it is the high magnitude of the event, in conjunction with the relatively low noise level at station WRAB in the year 2020 (Lecocq et al., 2020), that lead to this low Sv event producing an observable shear-coupled P-wave.

Signal-to-noise ratio of each event plays a roll in the disagreement between observability and our Sv control. In the case of the events with high Sv coefficients that do not produce observable shear-coupled P-waves, we suspect low signal-to-noise ratios drown out the arrivals. For these events, the magnitude and source distance could impact observability because smaller events recorded at greater epicentral distances produce smaller amplitude arrivals. If the amplitude of the arriving shear-coupled P-waves are below the ambient noise level at the recording station, the arrivals will not be observed, despite compliance with the other previously discussed controls. In the case of low Sv events that do produce shear-coupled P-waves within our data, we suspect similar signal-to-noise ratio complications. An event with a low, but nonzero, Sv coefficient can produce shear-coupled P-waves if the magnitude of the source event is high and the source distance is relatively low. Though the majority of the incoming shear wave energy from these events does not arrive in the radial-vertical plane, the energy that does arrive within the radial-vertical plane can be recorded above the ambient noise level.

We also note a consequence of our depth control. Because we favor events originating from greater depths, the events that generate shear-coupled P-waves generally come from subduction zones, resulting in limited azimuthal windows sampled by these phases. In both our data (Figure 4.9) and the findings of Thompson et al.

(2019), all shear-coupled P-waves observed at station WRAB have back azimuths associated with two subduction zones (the Java subduction zone to the north and the Tonga-Fiji subduction zone to the east), meaning that in the case of station WRAB, crustal properties can only be informed by shear-coupled P-waves to the north and east of the station.

Finally, the presence of *SpPmpPms,* as opposed to *SsPmpPmp*, within our data for event 2020-11-11 (Figure 4.13 & Figure 4.14) raises questions concerning the relative amplitudes of coincident crustal multiples, as we expect once converted phases to arrive at larger amplitudes than multiply converted phases. While we speculate that the angle of incidence for the rays associated with these phases plays a role in the observed amplitudes of these phases, future research is need to explain the presence of these shear arrivals.

Taking these limitations into account, the general agreement between our sweet spot maps (Figure 4.7 & Figure 4.8) and data (Table 2) show that our controls are useful in predicting the approximate number of shear-coupled P-wave arrivals various parts of the globe can expect annually. For future studies that utilize shear-coupled P-waves, our controls and sweet spot method can be used to determine ideal regions for data collection.

Conclusions

Our results show that the locations where shear-coupled P-waves can be observed, and subsequently utilized to resolve models of the earth's interior, are determined by source distance, magnitude, and depth, as well as the polarization of the incoming mantle S-wave. In order to determine the values of these controls, we utilize real data, synthetics, differential travel time curves, and a custom mapping method for visualizing the polarization of mantle shear waves (sweet spot maps). Our travel time curves, synthetics, and previously reported observations show that selecting events with source depths greater than 100km and source distances between 32 and 55 degrees, we ensure that we observe totally internally reflected rays that are not complicated by depth phases. Additionally, our sweet spot maps, in combination with real data and synthetics, show that selecting larger events and searching where incoming S-waves are more vertically polarized (higher Sv coefficient), we increase the likelihood of observing shear-coupled P-waves within recorded waveforms, as more energy can be converted from mantle S-waves to crustal P-waves.

Collecting a decade's worth of events and visualizing them in a sweet spot map, we identify regions on the globe that are most likely to record shear-coupled P-waves (Figure 4.7). The earthquakes that satisfy these controls usually originate from subduction zones, where the downgoing slab can create earthquakes at greater depths. This visualization seems to indicate that certain locations on the globe, typically within

32 to 55 degrees of a major subduction zone, are ideal for studies making use of shear-coupled P-waves. These locations include Australia, East Asia, Papua New Guinea, and parts of Antarctica.

Selecting Australia as our region of study, we verify these findings by collecting a year's worth of events that comply with our controls. During the year 2020, we find over 20 recordings of shear-coupled P-waves, which validates our findings in our global sweet spot map (Figure 4.7) and supports the values we select for our controls. While we do note the need for further investigation of the relationship between the Sv coefficient, source distance, and magnitude, our results show that the controls we select can be used to improve data collection for future studies.

References

Clitheroe, G., Gudmundsson, O., & Kennett, B. L. (2000). The crustal thickness of Australia. *Journal of Geophysical Research: Solid Earth*, *105*(B6), 13697–13713. https://doi.org/10.1029/1999jb900317

Crotwell, H. P., Owens, T. J., & Ritsema, J. (1999). The Taup Toolkit: Flexible Seismic Travel-time and Ray-Path Utilities. *Seismological Research Letters*, *70*(2), 154–160. https://doi.org/10.1785/gssrl.70.2.154

Dziewonski, A. M., Chou, T.-A., & Woodhouse, J. H. (1981). Determination of earthquake source parameters from waveform data for studies of global and regional seismicity. *Journal of Geophysical Research: Solid Earth*, *86*(B4), 2825–2852. https://doi.org/10.1029/jb086ib04p02825

Ekström, G., Nettles, M., & Dziewoński, A. M. (2012). The global CMT project 2004–2010: Centroid-moment tensors for 13,017 earthquakes. *Physics of the Earth and Planetary Interiors*, *200-201*, 1–9. https://doi.org/10.1016/j.pepi.2012.04.002

Gangopadhyay, A., Pulliam, J., & Sen, M. K. (2007). Waveform modelling of teleseismic*s*, SP, SSPMP, and shear-coupled pl waves for crust- and upper-mantle velocity structure beneath Africa. *Geophysical Journal International*, *170*(3), 1210–1226. https://doi.org/10.1111/j.1365-246x.2007.03470.x

IU: Global Seismograph Network - Iris/USGS. FDSN: IU: Global Seismograph Network - IRIS/USGS. (n.d.). Retrieved April 19, 2022, from https://doi.org/10.7914/SN/IU

Jordan, T. H., & Frazer, L. N. (1975). Crustal and upper mantle structure from*sp*phases. *Journal of Geophysical Research*, *80*(11), 1504–1518. https://doi.org/10.1029/jb080i011p01504

Kennett, B. L., Engdahl, E. R., & Buland, R. (1995). Constraints on seismic velocities in the Earth from traveltimes. *Geophysical Journal International*, *122*(1), 108–124. https://doi.org/10.1111/j.1365-246x.1995.tb03540.x

Lecocq, T., Hicks, S. P., Van Noten, K., van Wijk, K., Koelemeijer, P., De Plaen, R. S., Massin, F., Hillers, G., Anthony, R. E., Apoloner, M.-T., Arroyo-Solórzano, M., Assink, J. D., Büyükakpınar, P., Cannata, A., Cannavo, F., Carrasco, S., Caudron, C., Chaves, E. J., Cornwell, D. G., … Xiao, H. (2020). Global quieting of high-frequency seismic noise due to covid-19 pandemic lockdown measures. *Science*, *369*(6509), 1338–1343. https://doi.org/10.1126/science.abd2438

Liu, T., Klemperer, S. L., Yu, C., & Ning, J. (2020). Post-critical SSPMP and its applications to virtual deep seismic sounding (VDSS)—3: Back-projection imaging of the crust–mantle boundary in a heterogeneous lithosphere, theory and application. *Geophysical Journal International*, *223*(3), 2166–2187. https://doi.org/10.1093/gji/ggaa332

Nolet, G. (1983). Seismic wave propagation in stratified media B. L. N. Kennett, Cambridge University Press, 1983 x + 342 pp., 30.00. *Geophysical Journal International*, *75*(2), 573–573. https://doi.org/10.1093/astrogeo/75.2.573

Ou, G.-B. (2008). Seismological studies for tensile faults. *Terrestrial, Atmospheric and Oceanic Sciences*, *19*(5), 463. https://doi.org/10.3319/tao.2008.19.5.463(t)

Owens, T. J., & Zandt, G. (1997). Implications of crustal property variations for models of Tibetan Plateau Evolution. *Nature*, *387*(6628), 37–43. https://doi.org/10.1038/387037a0

Owens, T. J., Crotwell, H. P., Groves, C., & Oliver-Paul, P. (2004). SOD: Standing order for data. *Seismological Research Letters*, *75*(4), 515–520. https://doi.org/10.1785/gssrl.75.4.515-a

Pulliam, J., Sen, M. K., & Gangopadhyay, A. (2008). Waveform modeling of the crust and upper mantle using S, SP, SSPMP, and shear-coupled PL Waves. https://doi.org/10.21236/ada485986

Randall, G. E. (1994). Efficient calculation of complete differential seismograms for laterally homogeneous Earth models. *Geophysical Journal International*, *118*(1), 245–254. https://doi.org/10.1111/j.1365-246x.1994.tb04687.x

TA: USARRAY transportable array. FDSN: TA: USArray Transportable Array. (n.d.). Retrieved April 19, 2022, from https://doi.org/10.7914/SN/TA

Thompson, D. A., Rawlinson, N., & Tkalčić, H. (2019). Testing the limits of virtual deep seismic sounding via new crustal thickness estimates of the Australian continent. *Geophysical Journal International*, *218*(2), 787–800. https://doi.org/10.1093/gji/ggz191

Tseng, T.-L., Chen, W.-P., & Nowack, R. L. (2009). Northward thinning of Tibetan crust revealed by Virtual Seismic Profiles. *Geophysical Research Letters*, *36*(24). https://doi.org/10.1029/2009gl040457

Wessel, P., Luis, J. F., Uieda, L., Scharroo, R., Wobbe, F., Smith, W. H., & Tian, D. (2019). The generic mapping tools version 6. *Geochemistry, Geophysics, Geosystems*, *20*(11), 5556–5564. https://doi.org/10.1029/2019gc008515

Yu, Z., Ni, S., Wei, S., Zeng, X., Wu, W., & Li, Z. (2012). An iterative algorithm for separation of*s*and*scs*waves of great earthquakes. *Geophysical Journal International*, *191*(2), 591–600. https://doi.org/10.1111/j.1365-246x.2012.05603.x

Zandt, G., & Randall, G. E. (1985). Observations of shear-coupled P waves. *Geophysical Research Letters*, *12*(9), 565–568. https://doi.org/10.1029/gl012i009p00565

Zielhuis, A., & Hilst, R. D. (1996). Upper-mantle shear velocity beneath eastern Australia from inversion of waveforms from skippy portable arrays. *Geophysical Journal International*, *127*(1), 1–16. https://doi.org/10.1111/j.1365-246x.1996.tb015